



UNIVERSITÀ DEGLI STUDI DI PERUGIA

Dipartimento di Ingegneria

Laurea Magistrale in  
Ingegneria Informatica e Robotica

Enhancing Data Generation for  
Offline Reinforcement Learning through  
Causal Inference

Relatori:

**Prof. Gabriele Costante**  
**Dott. Raffaele Brilli**

Candidato:

**Paolo Speziali**

# Abstract

## English Version

This thesis addresses the challenges of data scarcity and noisy datasets in machine learning, with a focus on offline deep reinforcement learning. We introduce two novel frameworks for counterfactual data generation: WRe-CTDG and S-CTDG. These methods aim to augment pre-collected datasets by generating additional high-fidelity experiences that align with the environment's underlying transition dynamics. We evaluate our frameworks across various environments, comparing their performance against non-augmented baselines. Results demonstrate significant improvements in reinforcement learning performance, particularly for S-CTDG in complex environments, at the same time identifying important trade-offs regarding its applicability. This work contributes to the integration of causal inference and machine learning, offering new approaches to leverage causal relationships in data augmentation for offline deep reinforcement learning.

## Versione Italiana

Questa tesi affronta le sfide della scarsità di dati e dei dataset rumorosi nel machine learning, con un'attenzione particolare all deep reinforcement learning offline. Introduciamo due nuovi framework per la generazione di dati counterfactual: WRe-CTDG e S-CTDG. Questi sistemi mirano ad aumentare i dataset raccolti a priori generando esperienze aggiuntive ad alta fedeltà che si allineano alle dinamiche di transizione dell'ambiente. Abbiamo valutato i nostri framework in vari ambienti, confrontando le loro prestazioni con quelle di base senza aumento dei campioni. I risultati dimostrano miglioramenti significativi nelle prestazioni, in particolare per S-CTDG in ambienti più complessi, indentificandone allo stesso tempo importanti compromessi per quanto riguarda la sua applicabilità. Questo lavoro contribuisce all'integrazione dell'inferenza causale nel machine learning, offrendo nuovi approcci per sfruttare le relazioni causali nell'aumento dei dati per il deep reinforcement learning offline.

# Contents

<b>1</b>	<b>Introduction</b>	<b>6</b>
1.1	Data Scarcity and Noisy Datasets in Machine Learning . . . . .	7
1.2	Thesis Overview . . . . .	8
<b>2</b>	<b>State of the Art</b>	<b>9</b>
2.1	Offline RL: Advancements and Challenges . . . . .	10
2.1.1	Improving Robustness and Sample Efficiency . . . . .	10
2.1.2	Developing Datasets and Benchmarks . . . . .	10
2.2	Data Augmentation Strategies in RL . . . . .	11
2.2.1	Augmentation in Online and Offline RL . . . . .	11
2.2.2	Dynamics-Aware Augmentation . . . . .	12
2.3	Learning-Based Approaches to Data Generation . . . . .	12
2.3.1	Transformer-Based Models . . . . .	12
2.3.2	World Models and Variational Autoencoders . . . . .	12
2.4	Counterfactual Reasoning in Data Generation . . . . .	13
2.4.1	Counterfactual Generative Models . . . . .	13
2.4.2	Counterfactual Data Augmentation in Offline RL . . . . .	14
<b>3</b>	<b>Theoretical Background</b>	<b>16</b>
3.1	Deep Learning . . . . .	17
3.1.1	Convolutional Neural Networks . . . . .	19
3.2	Reinforcement Learning . . . . .	20
3.2.1	Reinforcement Learning Algorithms . . . . .	23
3.3	Generative Adversarial Networks . . . . .	25
3.3.1	Bidirectional GANs . . . . .	27
3.3.2	Bidirectional Conditional GANs . . . . .	28
3.3.3	Wasserstein GANs . . . . .	29
3.4	Causal Inference . . . . .	30
3.4.1	Correlation does not imply Causation . . . . .	30
3.4.2	The Flow of Association and Causation in Graphs . . . . .	31
3.4.3	Potential Outcomes and the Fundamental Problem of Causal Inference . . . . .	35
3.4.4	Causal Models and Identification . . . . .	37
3.4.5	Structural Causal Models . . . . .	40

<b>4 Methodology</b>	<b>42</b>
4.1 Problem Statement . . . . .	43
4.2 Simulation Environments . . . . .	45
4.2.1 Robotics Environments . . . . .	45
4.2.2 Healthcare Environments . . . . .	49
4.3 Frameworks for Counterfactual Data Generation . . . . .	52
4.3.1 Wasserstein Reward-enhanced CounTerfactual Data Generation . . . . .	52
4.3.2 Supervised CounTerfactual Data Generation . . . . .	56
<b>5 Experiments</b>	<b>59</b>
5.1 Hardware Specifications . . . . .	60
5.2 Software Environment . . . . .	60
5.3 Network Architectures Details . . . . .	60
5.3.1 WRe-CTDG Network Structure . . . . .	60
5.3.2 S-CTDG Network Structure . . . . .	62
5.3.3 Reinforcement Learning Algorithms (D3QN and TD3) . . . . .	63
5.4 Training Process Details . . . . .	64
5.4.1 Dataset Generation . . . . .	64
5.4.2 Counterfactual Data Generation . . . . .	65
5.4.3 Reinforcement Learning Training . . . . .	65
5.5 Results . . . . .	66
5.5.1 Training the Variational Autoencoder . . . . .	66
5.5.2 Reconstruction Loss During Generation . . . . .	67
5.5.3 Reinforcement Learning Performance . . . . .	69
5.6 Discussion and Analysis of Results . . . . .	72
<b>6 Conclusion</b>	<b>73</b>
6.1 Summary of Findings . . . . .	74
6.2 Implications and Contributions . . . . .	74
6.3 Limitations . . . . .	74
6.4 Future Research Directions . . . . .	75

# List of Figures

2.1	ImageNet Counterfactuals produced by the CGN . . . . .	14
2.2	The proposed Deep Generative Model for Counterfactual Data Augmentation in Offline RL . . . . .	14
3.1	A feed-forward neural network with two hidden layers . . . . .	17
3.2	A typical CNN architecture for classification. . . . .	19
3.3	A simple reinforcement learning task . . . . .	20
3.4	The example grid as a Markov Process graph, where the nodes represent the states and the edges represent the state transitions. . . . .	23
3.5	Partial taxonomy of algorithms in modern RL. . . . .	24
3.6	GAN framework applied to human faces generation task . . . . .	26
3.7	BiGAN architecture with generator, discriminator, and encoder. . . . .	27
3.8	BiCoGAN architecture with generator, discriminator, and encoder. . . . .	29
3.9	A confounding variable causes both wearing shoes to bed and waking up with a headache. . . . .	31
3.10	Different relationships between variables in a graph based on the assumptions. . . . .	32
3.11	Graph with two unassociated nodes. . . . .	32
3.12	Graph with two nodes $X_1$ and $X_2$ with an arrow from $X_1$ to $X_2$ , indicating that $X_1$ is a cause of $X_2$ . . . . .	33
3.13	Building blocks of DAGs: chain, fork, and immorality. . . . .	33
3.14	Blocked paths in chain and fork graphs. . . . .	34
3.15	Immorality with a blocked path and an unblocked path. . . . .	34
3.16	Conditioning on a descendant of a collider. . . . .	34
3.17	Potential outcomes for a causal effect. . . . .	36
3.18	The difference between observational and interventional distributions. . . . .	37
3.19	Randomized Controlled Trial (RCT) design vs. Observational Study. . . . .	37
3.20	Intervention as edge deletion in causal graphs. . . . .	39
3.21	Backdoor paths blocked by conditioning on $W$ . . . . .	40
3.22	Graph of 3.18. The dashed node $U$ means that $U$ is unobserved. . . . .	40
3.23	Graph of 3.19. . . . .	41
4.1	SCMs for the robotics environments. . . . .	46
4.2	SCMs and association rules. . . . .	46

4.3	Screenshot of the Acrobot environment with information about the state. . . . .	47
4.4	Screenshot of the Half Cheetah environment. . . . .	48
4.5	Screenshot of the Ant environment. . . . .	49
4.6	Structural Causal Model for the diabetes dataset. . . . .	50
4.7	Tree diagram of the expected numbers along each branch for the distribution from which the diabetes dataset was generated. . . . .	51
4.8	WRe-CTDG framework in a situation where the states are images only and the CAE is employed. . . . .	53
4.9	S-CTDG framework in a situation where the states are images only. .	56
5.1	Acrobot Reconstruction . . . . .	66
5.2	Half Cheetah Reconstruction . . . . .	67
5.3	Ant Reconstruction . . . . .	67
5.4	S-CTDG results for the Acrobot environment . . . . .	68
5.5	S-CTDG results for the Half Cheetah environment . . . . .	68
5.6	S-CTDG results for the Ant environment . . . . .	69
5.7	Acrobot Reward Trends . . . . .	70
5.8	Half Cheetah Reward Trends . . . . .	70
5.9	Ant Reward Trends . . . . .	71
5.10	Diabetes Reward Trends . . . . .	71

# Chapter 1

## Introduction

## 1.1 Data Scarcity and Noisy Datasets in Machine Learning

**Machine Learning** (ML) is reshaping our world in ways both subtle and profound. From the personalized recommendations we receive on streaming platforms to the autonomous vehicles navigating in real streets, ML algorithms are becoming an integral part of our daily lives. Yet, as these systems tackle increasingly complex challenges, they reveal their limitations. One of the most pressing issues is the critical need for large, high-quality datasets, a requirement that is often difficult to meet in real-world scenarios.

The **scarcity** of comprehensive datasets poses a significant obstacle in many fields, including healthcare and robotics. In **healthcare**, privacy concerns and limited access to patient records hinder the collection of diverse and extensive data. Similarly, in **robotics**, certain experimental data may be difficult or costly to obtain, particularly in scenarios involving complex physical interactions or rare events. This data scarcity can lead to underfitted or non-generalizable models, compromising their accuracy and utility in practical applications.

Moreover, even when substantial datasets are available, they often suffer from **noise and inconsistencies**. Real-world data collection processes are rarely perfect, resulting in datasets that may contain outliers or biased samples, also due to unmeasured variables and confounding factors. These imperfections can significantly impact the performance of ML models, leading to unreliable predictions or decisions. The challenge of dealing with noisy datasets is particularly acute in offline **Deep Reinforcement Learning** (DRL) scenarios, where agents must learn optimal policies from pre-collected experiences without the ability to interact further with the environment.

To address these challenges, researchers have long employed **data augmentation techniques**. Traditional data augmentation methods involve applying various transformations to existing data points to artificially expand the dataset. In image processing, for instance, this might involve rotations, flips, or color adjustments. While these techniques have proven effective in many applications, they have limitations. Notably, not all transformations produce valid or realistic data points, especially in domains with complex underlying structures or causal relationships.

This is where the integration of **Causal Inference** into ML frameworks offers a promising solution. Causal inference focuses on understanding the cause-and-effect relationships between variables, rather than merely identifying correlations. By leveraging causal inference, we can develop more sophisticated data augmentation techniques that respect the underlying causal structure of the data-generating process.

In this thesis, we propose novel approaches to address the challenges of data scarcity and noisy datasets by leveraging causal inference techniques. We introduce two frameworks for counterfactual data generation: the **Wasserstein Reward-enhanced Counterfactual Data Generation** (WRe-CTDG) and the **Super-**

**vised Counterfactual Data Generation** (S-CTDG). These methods aim to augment pre-collected datasets by generating additional high-fidelity experiences that align with the environment’s underlying transition dynamics.

Our work focuses specifically on offline DRL scenarios, where agents are trained using pre-collected datasets of experiences, and we are going to explore applications in both robotics environments and healthcare scenarios.

By incorporating **Structural Causal Models** (SCMs) and **Generative Adversarial Networks** (GANs) into our frameworks, we develop techniques to infer causal relationships and generate counterfactual samples. This approach allows us to create synthetic data points that are not mere transformations of existing data, but rather plausible alternative scenarios that could have occurred under different circumstances. This is particularly valuable in offline DRL, where the ability to explore “what-if” scenarios can significantly enhance the robustness and generalization capabilities of learned policies.

## 1.2 Thesis Overview

The following chapters are organized as follows:

- In **Chapter 2**, we provide an overview of the State of the Art in Offline Reinforcement Learning, Data Augmentation and Generation Techniques, and Counterfactual Reasoning in Data Generation.
- In **Chapter 3**, we introduce the theoretical foundations of the technologies used in our proposed frameworks, including Structural Causal Models, Generative Adversarial Networks, and Deep Reinforcement Learning algorithms.
- In **Chapter 4**, we present the WRe-CTDG and the S-CTDG frameworks, detailing their architectures and training procedures. We also present the environments and datasets used for evaluation.
- In **Chapter 5**, we present a description of the machines specifications and of the details of the neural networks employed in our experiments, followed by a detailed overview of the experimental results.
- In **Chapter 6**, we discuss the implications of our findings, the limitations of our approaches, and potential directions for future research.

## Chapter 2

# State of the Art

## 2.1 Offline RL: Advancements and Challenges

**Offline Reinforcement Learning** (Offline RL) has emerged as a promising approach for training control policies using pre-collected experiences, eliminating the need for potentially dangerous or costly online interactions. Despite significant progress in this field, several challenges persist in its practical application, particularly in control and robotics domains.

Research efforts to enhance Offline RL performance are primarily advancing along two paths that we are now going to explore.

### 2.1.1 Improving Robustness and Sample Efficiency

The first research direction focuses on refining existing methods to enhance their robustness and sample efficiency. [Kumar et al., 2021] propose a comprehensive workflow for offline model-free robotic reinforcement learning. Their approach addresses challenges specific to real-world robotics applications, proposing metrics and protocols to assist practitioners in selecting policy checkpoints, regularization parameters, and model architecture.

[Shin and Kim, 2023] introduce a hierarchical approach called “Guide to Control” that solves efficiently long-horizon and sparse-reward tasks from offline data. This method enhances the effectiveness of offline RL in complex environments by breaking down the overall task into more manageable sub-tasks, thereby improving learning efficiency and performance.

### 2.1.2 Developing Datasets and Benchmarks

The second path concentrates on creating extensive datasets and benchmarks tailored for control and robotics domains. [Gürtler et al., 2023] present a benchmark for offline RL on real-robot hardware, providing a useful resource for evaluating algorithms in practical settings. In their work they propose a set of benchmark datasets for robotic manipulation that are intended to help improving the state-of-the-art in offline reinforcement learning.

[Liu et al., 2023] contribute datasets and benchmarks specifically designed for offline safe reinforcement learning to accelerate research in this area. Their work addresses the critical aspect of safety in robotic applications, providing resources for researchers to develop and test algorithms that not only optimize performance but also ensure safe operation in various scenarios. The suite comprises three main components: expertly crafted safe policies, D4RL-styled datasets with environment wrappers, and high-quality offline safe RL baseline implementations. The authors present a methodical data collection pipeline using advanced safe RL algorithms to generate diverse datasets across 38 popular safe RL tasks, ranging from robot control to autonomous driving. They also introduce data post-processing filters to modify dataset diversity, simulating various data collection conditions.

## 2.2 Data Augmentation Strategies in RL

Despite ongoing improvements in learning algorithms, the quantity of training data continues to be a critical determinant of success in machine learning processes. This is especially challenging when dealing with complex, high-dimensional inputs such as images, where the data requirements for effective training are substantial.

To address the problem of limited data availability, researchers and practitioners often turn to **data augmentation techniques**. These methods aim to expand existing datasets by generating synthetic samples that are both artificial and plausible, thereby enriching the training set without the need for additional real-world data collection.

[Mumuni and Mumuni, 2022] provide a comprehensive survey of modern data augmentation approaches, highlighting their potential in enhancing computer vision across various domains.

### 2.2.1 Augmentation in Online and Offline RL

Both online and offline RL approaches have incorporated data augmentation techniques to improve learning efficiency and generalization.

In the **online** RL setting, [Laskin et al., 2020] introduce Reinforcement Learning with Augmented Data (RAD), a simple module designed to enhance most RL algorithms. The authors conduct an extensive study of various data augmentation techniques for both pixel-based and state-based inputs in RL, including two new augmentations they introduce: random translate and random amplitude scale.

[Hansen and Wang, 2021] further explore the concept of data augmentation in online RL, proposing SOft Data Augmentation (SODA), a novel approach to improve generalization in RL; unlike traditional methods that directly learn policies from augmented data, SODA decouples augmentation from policy learning. It does this by applying a soft constraint on the encoder to maximize mutual information between latent representations of augmented and non-augmented data, while using only non-augmented data for RL optimization.

In the **offline** RL setting, [Han and Kim, 2022] introduce a selective data augmentation technique using a Variational Autoencoder.

A **Variational Autoencoder** (VAE), defined in [Kingma and Welling, 2022], is an unsupervised learning architecture that learns a low-dimensional latent space representation of the input data by encoding and decoding it through two separate neural networks.

The method of [Han and Kim, 2022] targets sparse subspaces in the dataset, representing them in the VAE's latent space, then sampling and decoding new data points to augment underrepresented regions. This approach aims to generate virtual data that closely aligns with the original data distribution.

[Joo et al., 2022] propose a data augmentation method for offline RL called Swapping Target Q-Value (SQV). SQV works by swapping Q-values between original and

transformed images, encouraging the algorithm to treat similar states as equivalent while emphasizing differences between distinct states. This method aims to enhance pixel-based learning without auxiliary loss functions, potentially improving performance and generalization in offline RL scenarios with limited datasets.

### 2.2.2 Dynamics-Aware Augmentation

Traditional augmentation methods often operate without knowledge of the underlying environment dynamics, requiring careful tuning to avoid generating inconsistent samples. To mitigate this issue, dynamics-aware augmentation schemes have emerged in the robotics field.

In a paper by [Lin et al., 2020] the authors introduce a framework called **Invariant Transform Experience Replay** to improve Deep Reinforcement Learning (DRL) for robot control. The main idea is to use symmetries in robotic tasks to create more training data by exploiting reflectional symmetries and taking advantage of flexible goal definitions.

Nonetheless, effectively implementing these techniques requires an in-depth understanding of the underlying process, which is often not available, and the development of an augmentation strategy specifically crafted for the task at hand.

## 2.3 Learning-Based Approaches to Data Generation

Researchers are increasingly turning to data-driven methods to overcome these obstacles. These approaches aim to learn the underlying data generation model from the offline dataset itself. After the model is trained, it can be used to produce new samples that align with the environment’s dynamics. This strategy allows for the creation of synthetic data that is more likely to be consistent with the real-world processes being modeled, without requiring explicit knowledge of those processes.

### 2.3.1 Transformer-Based Models

[Wang et al., 2022] introduce the Bootstrapped Transformer, a novel algorithm for offline RL. They approach offline RL as a sequence generation problem, using **Transformer** models to represent trajectories. Recognizing the common issue of limited and insufficiently diverse training data in offline RL datasets, they implement a **bootstrapping technique**: this allows the model to generate additional offline data using its own learned representations, which is then used to enhance the training of the sequence model.

### 2.3.2 World Models and Variational Autoencoders

**World Models**, introduced in [Ha and Schmidhuber, 2018], are a class of models that combine a Variational Autoencoder as a Vision module, a Recurrent Neural Network (RNN) with a Mixture Density Network (MDN) as a Memory module and

a simple Neural Network (NN) layer as a Controller. These models can be trained quickly in an unsupervised manner to learn a compressed spatial and temporal representation of the environment.

Despite not being explicitly designed for data augmentation, World Models and VAEs can be naturally used to achieve the same objective.

[Hafner et al., 2020] introduces **Dreamer**, a reinforcement learning agent that uses a learned world model to solve complex tasks from visual inputs. Dreamer learns a compact latent space representation of the environment and uses this model to imagine trajectories and learn behaviors through “latent imagination”. The agent learns both actions and state values in the latent space, efficiently optimizing behavior by propagating analytic gradients of learned state values through imagined trajectories.

A similar approach was proposed in [Andersen et al., 2018], where the **Dreaming Variational Autoencoder** (DVAE) architecture is presented. The DVAE combines variational autoencoders with deep reinforcement learning agents, allowing agents to learn optimal policies using generated training data samples. To test this approach, the authors also present **Deep Maze**, a novel and flexible maze engine that provides various challenges for reinforcement learning algorithms, including partial and fully-observable state-spaces, long-horizon tasks, and both deterministic and stochastic problems.

## 2.4 Counterfactual Reasoning in Data Generation

The **counterfactual-based approach** offers a versatile and robust alternative rooted in the theory of **Structural Causal Models** (SCMs) (which are discussed in more detail in Section 3.4.5). This method begins by modeling the system’s dynamics using an SCM, which is then employed for counterfactual reasoning. This process generates new samples as counterfactual outcomes that align with the model. Unlike previous methods, SCMs provide tools to model and estimate unmeasured variables, enabling a more precise depiction of the factors affecting the system’s behavior.

### 2.4.1 Counterfactual Generative Models

[Sauer and Geiger, 2021] introduce the **Counterfactual Generative Network** (CGN), a novel approach to improve the robustness and interpretability of image classifiers. The authors propose decomposing the image generation process into independent causal mechanisms that disentangle object shape, texture and background. This allows for the generation of counterfactual images, synthetic images with novel combinations of these features. The CGN is trained without direct supervision, using only class labels and inductive biases and the authors demonstrate the CGN’s ability to generate counterfactual images on MNIST and ImageNet datasets, as shown in Figure 2.1.

Another usage of counterfactual reasoning, this time in the context of medical

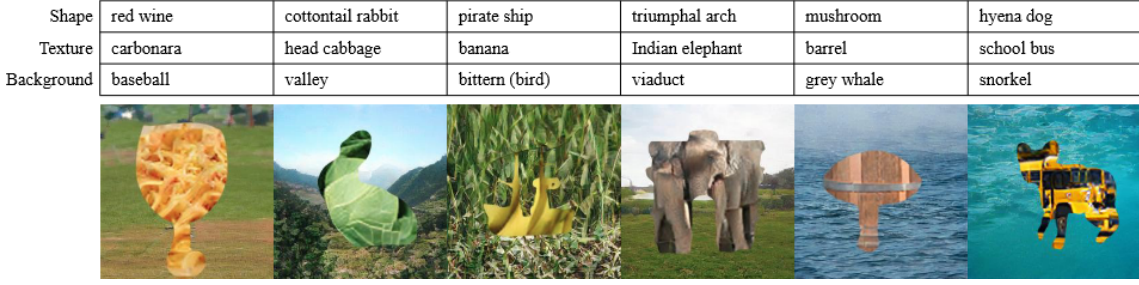


Figure 2.1: ImageNet Counterfactuals produced by the CGN

Source: [Sauer and Geiger, 2021]

imaging, is presented in [Mertes et al., 2022]. This paper introduces GANterfactual, a novel approach for generating counterfactual explanations for image classifiers using adversarial image-to-image translation techniques. Unlike traditional methods that highlight important areas in images, GANterfactual modifies input images to change the classifier’s prediction, providing users with a different kind of explanatory information. The authors focus on medical contexts, specifically pneumonia detection in chest X-rays, where textural and structural information is necessary.

#### 2.4.2 Counterfactual Data Augmentation in Offline RL

[Lu et al., 2020] investigate counterfactual-based data augmentation specifically in the context of Offline RL. They propose a Deep Generative Model based on the Bidirectional Conditional Generative Adversarial Network (BiCoGAN) architecture (which is discussed in more detail in Section 3.3.2), the model can be seen in Figure 2.2. The authors use SCMs to model state dynamics, leveraging both commonalities and differences across subjects, and allowing to estimate unmeasured variables, which are then used to effectively reproduce the environment’s initial conditions and enable the generation of counterfactual outcome. They prove that counterfactual outcomes are identifiable under mild conditions and that a Double Dueling Deep Q-Network (discussed in Section 3.2) trained on both the augmented dataset and the original counterpart achieves better performance on the first one.

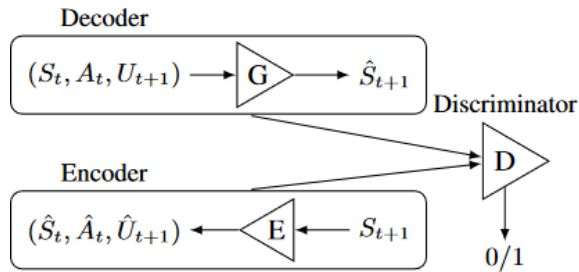


Figure 2.2: The proposed Deep Generative Model for Counterfactual Data Augmentation in Offline RL

Source: [Lu et al., 2020]

However, this approach is designed for non-visual, low-dimensional inputs, and discrete control actions. Additionally, a significant drawback of this algorithm is its lack of a mechanism for estimating the reward associated with the generated states. This limitation implies that retrieving the reward is possible only when the reward function can be directly calculated from the generated states, a condition that does not always apply.

## Chapter 3

# Theoretical Background

### 3.1 Deep Learning

In the field of machine learning, the first models you are often introduced to are those for regression and classification that utilize linear combinations of fixed basis functions. According to [Bishop, 2008], these models possess useful analytical and computational properties, but their practical applicability is constrained since their capacity is limited to linear functions and they cannot understand the interaction between any two input variables. This leads to problems such as the **curse of dimensionality**, where the number of possible interactions between variables grows exponentially with the number of input variables. To address large-scale problems, it is essential to adapt the basis functions to the data, as demonstrated by Support Vector Machines (SVMs). Alternatively, one can fix the number of basis functions in advance while allowing them to be adaptive, utilizing parametric forms for the basis functions with parameter values adjusted during training.

The most successful example of this approach in pattern recognition is the **feed-forward neural network**, also known as the **MultiLayer Perceptron** (MLP).

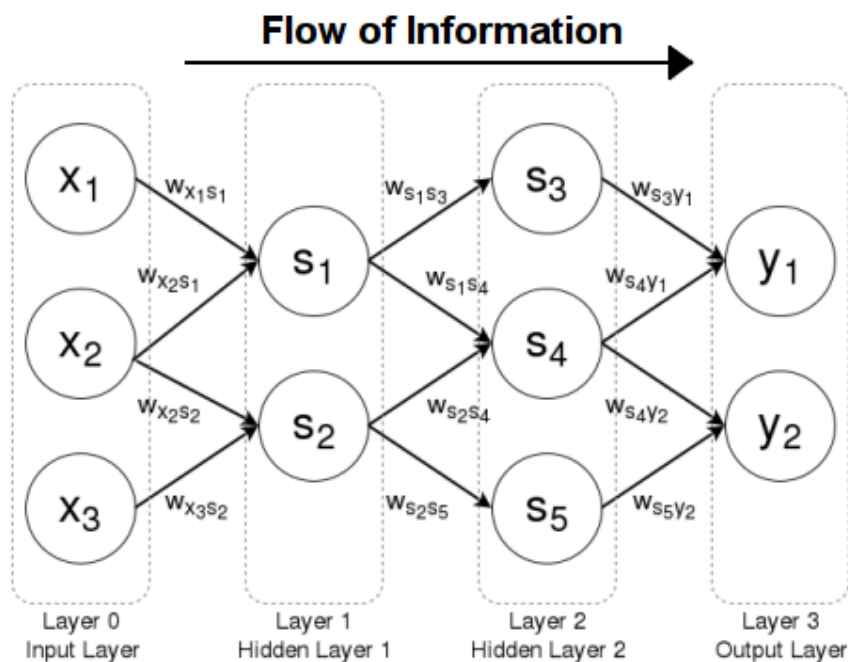


Figure 3.1: A feed-forward neural network with two hidden layers

Source: Brilliant

As explained in [Goodfellow et al., 2016], the goal of a feedforward network is to approximate a specific function  $f^*$ . For example, in a classification task,  $y = f^*(x)$  maps an input  $x$  to a category  $y$ . A feedforward network defines a mapping  $y = f(x; \theta)$  and learns the parameters  $\theta$  that yield the best approximation of this function.

These models are called **feedforward** because information flows unidirectionally from the input  $x$ , through intermediate computations defining  $f$ , and ultimately to the output  $y$ , without feedback loops.

The training data directly specifies the behavior of the output layer but not the intermediate layers, which are called **hidden layers** since their desired outputs are not provided by the training data. The learning algorithm must determine how to best utilize these hidden layers to approximate  $f^*$ . Every layer of the network computes a non-linear transformation of the previous layer's activations, this way a complex function can be approximated by composing simpler functions, one for each layer. Layers are composed of a set of **units**, where each unit is a node that computes a non-linear function of the weighted sum of its inputs and is only connected to units in the previous and the following layer.

In order to train the network and update the weights, MLPs use the **backpropagation** technique, which computes the gradient of the loss function with respect to the weights of the network. The weights are then updated using an optimization algorithm such as **Stochastic Gradient Descent** (SGD) or one of its adaptive variants like **Adam**, whose hyperparameters are tuned according to the task during training.

A feedforward network is called a **deep neural network** if it has more than one hidden layer, the branch of machine learning that studies deep neural networks is called **deep learning**.

They are called networks due to their structure, which involves composing multiple functions together. Typically, this composition is represented by a directed acyclic graph. For instance, functions  $f^{(1)}$ ,  $f^{(2)}$ , and  $f^{(3)}$  might be connected in a chain to form  $f(x) = f^{(3)}(f^{(2)}(f^{(1)}(x)))$ .

Functions  $f^{(1)}$  and  $f^{(2)}$  must be non linear, otherwise the composition would collapse into a single linear function. These non-linear functions are called **activation functions**. The last function  $f^{(3)}$  is typically a linear function that maps the output of the final hidden layer to the output layer. This is the same as applying a linear model to a transformed input  $\phi(x)$ , where  $\phi$  is a nonlinear transformation. The question then becomes how to choose the mapping  $\phi$ .

The strategy of deep learning is to learn  $\phi$ : in this approach, we use a model

$$y = f(x; \theta, w) = \phi(x; \theta)^\top w \quad (3.1)$$

Here, we have parameters  $\theta$  that are used to learn  $\phi$  from a broad class of functions, and parameters  $w$  that map  $\phi(x)$  to the desired output. This approach allows for greater flexibility: specifically, by using a broad family of functions  $\phi(x; \theta)$ , the human designer only needs to select the appropriate general function family rather than finding precisely an exact function.

The **universal approximation theorem** [Hornik et al., 1989] tells us that regardless of what function we are trying to learn, we know that a feedforward network with enough units will be able to *represent* this function, however we are not guaranteed that the training algorithm will be able to *learn* it.

### 3.1.1 Convolutional Neural Networks

**Convolutional Neural Networks** (CNNs) are a specialized type of neural network for processing data that has a known, grid-like topology, it is particularly effective for image recognition tasks.

The key components of CNNs are:

- **Convolutional layers:** These layers apply a convolution operation to the input, passing the result to the next layer. The input grid is convolved with a set of filters, also known as **kernels**, which are small windows that move across the input grid and apply a convolution operation between the input and the kernel weight at each position. The weight of the kernel is learned during training. Each convolutional layer applies multiple filters to the input, each producing a different **feature map**.
- **Pooling layers:** These layers downsample the feature maps produced by the convolutional layers to reduce the dimensionality of the data. This reduces the computational complexity of the network and helps to focus on the most important elements of the input.
- **Fully connected (FC) layers:** These layers connect every neuron in one layer to every neuron in another layer. It is in these layers that the features learned by the convolutional layers are used to classify the input image.

An example of a CNN classification architecture is shown in Figure 3.2.

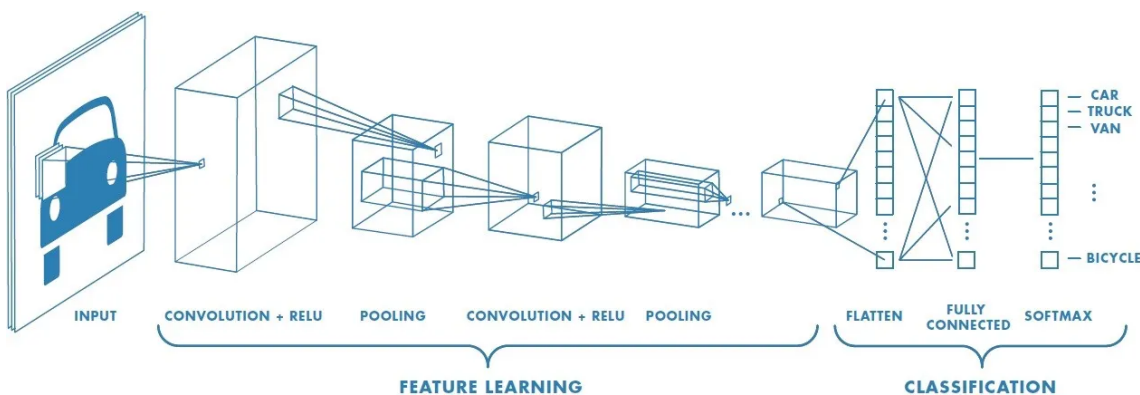


Figure 3.2: A typical CNN architecture for classification.

Source: Sumit Saha

CNNs have been shown to achieve state-of-the-art performance on a variety of computer vision tasks, including image classification, object detection and image segmentation. They have also been successfully applied to other types of data, such as speech recognition and natural language processing.

## 3.2 Reinforcement Learning

“**Reinforcement learning** is learning [...] how to map situations to actions so as to maximize a numerical reward signal. The learner is not told which actions to take, but instead must discover which actions yield the most reward by trying them. In the most interesting and challenging cases, actions may affect not only the immediate reward but also the next situation and, through that, all subsequent rewards. These two characteristics, **trial-and-error search** and **delayed reward**, are the two most important distinguishing features of reinforcement learning.” [Sutton and Barto, 1998]

Let’s explore the basic concepts of reinforcement learning with a simple example as described in [Zhao, 2024]. Consider a grid world scenario as shown in Figure 3.3 where a robot, referred to as the **agent**, moves between cells, occupying one cell at a time. The white cells are accessible, while the orange cells are forbidden. The goal is for the agent to reach a target cell.

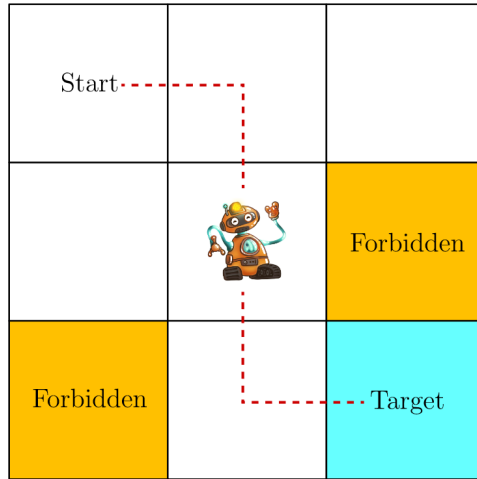


Figure 3.3: A simple reinforcement learning task

Source: [Zhao, 2024]

To achieve this, the agent needs a **policy** that guides it to the target efficiently, avoiding forbidden cells and unnecessary detours. If the grid layout is known, planning is simple. However, without prior knowledge, the agent must explore and learn through trial and error.

The agent’s status in the grid is defined by its **state**  $s_i \in \mathcal{S}$ , which represents its location relative to the **environment**. In the examples with nine cells, the state space is  $\mathcal{S} = \{s_1, s_2, \dots, s_9\}\dots$

From each state, the agent can perform five **actions**: move up, right, down, left or stay put, denoted as  $a_1, a_2, \dots, a_5$ , this set of actions is the action space  $\mathcal{A} = \{a_1, \dots, a_5\}$ . The available actions can vary by state, for instance, at  $s_1$ , actions  $a_1$  (up) and  $a_4$  (left) would collide with the grid boundary, so the action space is  $\mathcal{A}(s_1) = \{a_2, a_3, a_5\}\dots$

When taking an action, the agent may move from one state to another, a process known as **state transition**. For example, if the agent is at state  $s_1$  and selects action  $a_2$  (moving rightward), it transitions to state  $s_2$ . This process can be represented as:

$$s_1 \xrightarrow{a_2} s_2$$

The state transition process is defined for each state and its associated actions. Mathematically, state transitions are described by conditional probabilities. For example, for  $s_1$  and  $a_2$ , the conditional probability distribution is:

$$\begin{aligned} p(s_1 | s_1, a_2) &= 0, \\ p(s_2 | s_1, a_2) &= 1, \\ p(s_3 | s_1, a_2) &= 0, \\ p(s_4 | s_1, a_2) &= 0, \\ p(s_5 | s_1, a_2) &= 0, \end{aligned}$$

indicating that taking  $a_2$  at  $s_1$  guarantees the agent moves to  $s_2$ , with a probability of one, and zero probability for other states.

This is a deterministic state transition, but state transitions can also be stochastic, requiring conditional probability distributions. For instance, if random wind gusts affect the grid, taking action  $a_2$  at  $s_1$  might blow the agent to  $s_5$  instead of  $s_2$ , resulting in  $p(s_5 | s_1, a_2) > 0$ .

A **policy** is a function that maps states to actions, indicating the agent's behavior in the environment. In other words, a policy tells the agent what action to take at each state.

Mathematically, policies can be described by conditional probabilities. For example, the policy for  $s_1$  is:

$$\begin{aligned} \pi(a_1 | s_1) &= 0, \\ \pi(a_2 | s_1) &= 1, \\ \pi(a_3 | s_1) &= 0, \\ \pi(a_4 | s_1) &= 0, \\ \pi(a_5 | s_1) &= 0, \end{aligned}$$

indicating that the probability of taking action  $a_2$  at state  $s_1$  is one, and the probabilities of taking other actions are zero.

The above policy is deterministic, but policies may generally be stochastic. For instance, let's assume that at state  $s_1$  the agent may take actions to move either rightward or downward, each with a probability of 0.5. In this case, the policy for  $s_1$  is:

$$\begin{aligned} \pi(a_1 | s_1) &= 0, \\ \pi(a_2 | s_1) &= 0.5, \\ \pi(a_3 | s_1) &= 0.5, \\ \pi(a_4 | s_1) &= 0, \\ \pi(a_5 | s_1) &= 0. \end{aligned}$$

After executing an action at a state, the agent receives a reward  $r$  as feedback from the environment. The **reward** is a function of the state and action which predicts immediate reward and is denoted as:

$$R(s_t = s, a_t = a) = \mathbb{E}[r_t | s_t = s, a_t = a] \quad (3.2)$$

and it can be positive, negative, or zero. Different rewards influence the policy the agent learns. Generally, a positive reward encourages the agent to take the corresponding action, while a negative reward discourages it.

However we can't find good policies by simply selecting actions with the greatest immediate rewards since they do not consider long-term outcomes. To determine a good policy, we must consider the total reward obtained in the long run and an action with the highest immediate reward may not lead to the greatest total reward.

A **trajectory** is a state-action-reward chain. For example, the agent in our example may follow this trajectory:

$$s_1 \xrightarrow{a_2, r=0} s_2 \xrightarrow{a_3, r=0} s_5 \xrightarrow{a_3, r=0} s_8 \xrightarrow{a_2, r=1} s_9.$$

The **return** of this trajectory is the sum of all rewards collected along it, in the example above:

$$\text{return} = 0 + 0 + 0 + 1 = 1$$

Returns, also called total rewards or cumulative rewards, are used to evaluate policies. Returns can also be defined for infinitely long trajectories, which may diverge. Therefore, we introduce the concept of **discounted return** for infinitely long trajectories. The discounted return is the sum of the rewards from  $t$  to  $T$  (final step):

$$G_t \doteq R_{t+1} + \gamma R_{t+2} + \gamma^2 R_{t+3} + \dots = \sum_{k=0}^{\infty} \gamma^k R_{t+k+1} \quad (3.3)$$

where  $\gamma \in [0, 1]$  is the **discount factor**. If  $\gamma$  is close to 0, the agent emphasizes near-future rewards, resulting in a short-sighted policy. If  $\gamma$  is close to 1, the agent emphasizes far-future rewards.

When  $T$  is finite, we call the task episodic and each sequence up to the **terminal state** is an **episode**. Otherwise, we refer to **continuing tasks**.

The **Markov Decision Processes** (MDPs), a general framework for describing stochastic dynamical systems, allows us to formally presents these concepts. The **Markov property** refers to the **memoryless** property of a stochastic process. Mathematically, it means that

$$\begin{aligned} p(s_{t+1} | s_t, a_t, s_{t-1}, a_{t-1}, \dots, s_0, a_0) &= p(s_{t+1} | s_t, a_t), \\ p(r_{t+1} | s_t, a_t, s_{t-1}, a_{t-1}, \dots, s_0, a_0) &= p(r_{t+1} | s_t, a_t), \end{aligned} \quad (3.4)$$

where  $t$  represents the current time step and  $t + 1$  represents the next time step. This indicates that the next state or reward depends only on the current state and action and is independent of the previous ones.

An MDP is defined by a tuple  $\langle \mathcal{S}, \mathcal{A}, P, R, \gamma \rangle$ , let us break down the components:

- $\mathcal{S}$ : finite set of Markov states  $s$
- $\mathcal{A}$ : finite set of actions  $a$
- $P$ : state transition model for each action, a probability matrix that specifies

$$p(s_t + 1 = s' | s_t = s, a_t = a)$$

- $R$ : reward function

$$R(s_t = s, a_t = a) = \mathbb{E}[r_t | s_t = s, a_t = a]$$

- $\gamma$ : discount factor  $0 \leq \gamma \leq 1$

When the policy in a MDP is fixed, it reduces to a **Markov Process** (MP), this transformation simplifies the MDP by eliminating the decision-making aspect. A Markov process is referred to as a **Markov Chain** if it operates in discrete time and the number of states is either finite or countable.

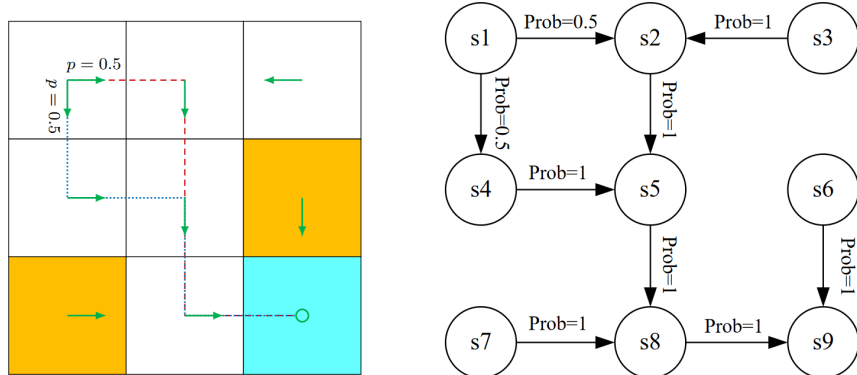


Figure 3.4: The example grid as a Markov Process graph, where the nodes represent the states and the edges represent the state transitions.

Source: [Zhao, 2024]

### 3.2.1 Reinforcement Learning Algorithms

In [OpenAI Inc., 2018], the landscape of algorithms in modern reinforcement learning is explored.

The algorithms used in reinforcement learning almost always rely on **value functions**. The **value** is the expected return if the agent starts in that state or state-action pair and then follows a specific policy indefinitely.

There are four primary value functions to consider:

- **On-Policy Value Function**,  $V^\pi(s)$ : This function represents the expected return if the agent starts in state  $s$  and acts according to the policy  $\pi$ :

$$V^\pi(s) = \mathbb{E}_{\tau \sim \pi} [R(\tau) \mid s_0 = s] \quad (3.5)$$

- **On-Policy Action-Value Function**,  $Q^\pi(s, a)$ : This function gives the expected return if the agent starts in state  $s$ , takes an arbitrary action  $a$ , and then always follows the policy  $\pi$ :

$$Q^\pi(s, a) = \mathbb{E}_{\tau \sim \pi} [R(\tau) \mid s_0 = s, a_0 = a] \quad (3.6)$$

- **Optimal Value Function**,  $V^*(s)$ : This function provides the expected return if the agent starts in state  $s$  and follows the optimal policy for the environment:

$$V^*(s) = \max_{\pi} \mathbb{E}_{\tau \sim \pi} [R(\tau) \mid s_0 = s] \quad (3.7)$$

- **Optimal Action-Value Function**,  $Q^*(s, a)$ : This function represents the expected return if the agent starts in state  $s$ , takes an arbitrary action  $a$ , and then follows the optimal policy for the environment:

$$Q^*(s, a) = \max_{\pi} \mathbb{E}_{\tau \sim \pi} [R(\tau) \mid s_0 = s, a_0 = a] \quad (3.8)$$

Figure 3.5 presents a partial taxonomy of the modern reinforcement learning algorithms. One key distinction is whether the agent utilizes (or learns) a model of the environment. A model, in this context, refers to a function that predicts state transitions and rewards.

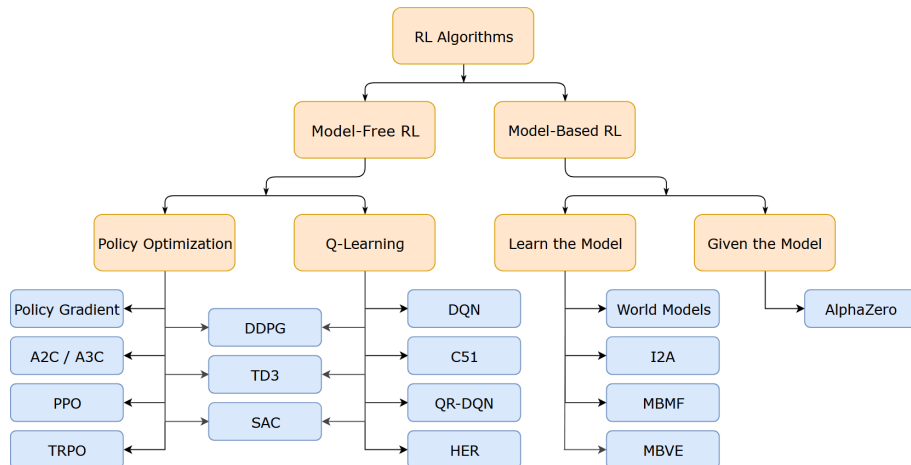


Figure 3.5: Partial taxonomy of algorithms in modern RL.

Source: [OpenAI Inc., 2018]

The primary advantage of having a model is that it enables the agent to plan by predicting future states and rewards. However, the major drawback is that an accurate model of the environment is often unavailable to the agent. Algorithms which use a model are known as **model-based** methods, while those that do not are referred to as **model-free** methods. Our focus will be on the latter.

Model-free methods can be categorized into two main approaches for representing and training agents:

- **Policy Optimization:** explicitly represents a policy as  $\pi_\theta(a | s)$  and optimizes the parameters  $\theta$  either directly via gradient ascent on the performance objective  $J(\pi_\theta)$  or indirectly by maximizing local approximations of  $J(\pi_\theta)$ . Typically, this optimization is performed **on-policy**, meaning that each update uses data collected while the agent is acting according to the most recent version of the policy.
- **Q-Learning:** involves learning an approximator  $Q_\theta(s, a)$  for the optimal action-value function  $Q^*(s, a)$ . Unlike policy optimization, Q-learning is generally performed **off-policy**, allowing updates to use data collected at any time during training, irrespective of the agent's policy at the time of data collection. The corresponding policy is derived from the relationship between  $Q^*$  and  $\pi^*$ , where the actions taken by the Q-learning agent are determined by

$$a(s) = \arg \max_a Q_\theta(s, a) \quad (3.9)$$

An example of a Q-learning algorithm is Deep Q-Network (**DQN**), which uses a deep neural network to approximate the optimal action-value function in environments with large state spaces [Mnih et al., 2013], and its variants such as Double DQN (**DDQN**) [van Hasselt et al., 2015] and Dueling Double DQN (**D3QN**) [Wang et al., 2016]. This family of algorithms is used in tasks with discrete action spaces.

There are also hybrid approaches that combine elements of both policy optimization and Q-learning. In this spectrum of algorithms we can find **actor-critic methods**, which consist of two components: an **actor** that makes actions and a **critic** that evaluates them. An example of an actor-critic algorithm is Twin-Delayed DDPG (**TD3**) [Fujimoto et al., 2018]. These methods are used in tasks with continuous action spaces.

If samples are collected during training the reinforcement learning is considered **online**, otherwise, if the training set is fixed, it is **offline**.

### 3.3 Generative Adversarial Networks

**Generative Adversarial Networks** (GANs) is a framework for estimating generative models via an adversarial process, initially introduced by [Goodfellow et al., 2014].

This framework involves training two models: a **generative** model  $G$ , which captures the data distribution, and a **discriminative** model  $D$ , which predicts samples as either originating from the true data distribution or the generative model. The training objective for  $G$  is to maximize the likelihood of  $D$  making incorrect classifications. This adversarial process can be conceptualized as a minimax two-player game. In the theoretical space of arbitrary functions  $G$  and  $D$ , a unique solution exists where  $G$  accurately recovers the training data distribution and  $D$  outputs  $\frac{1}{2}$  for all inputs (in other words, it reaches maximum uncertainty). When  $G$  and  $D$  are defined by multilayer perceptrons, the entire system can be trained using backpropagation.

To learn the generator's distribution  $p_G$  over data  $x$ , we define a prior  $p_z(z)$  on input noise variables  $z \in \Omega_Z$ , called **latent distribution**, and represent a mapping to the data space as  $G(z; \theta_g)$ , where  $G : \Omega_Z \rightarrow \Omega_X$  is a differentiable function parameterized by  $\theta_g$ . Additionally, we define a second network  $D(x; \theta_d)$  that outputs a single scalar, representing the probability that  $x$  originated from the true data distribution  $p_x$  rather than from  $p_G$ . The discriminative model  $D$  is trained to maximize the probability of correctly labeling both the training examples and the samples generated by  $G$ . Simultaneously, the generative model  $G$  is trained to minimize  $\log(1 - D(G(z)))$ .

Formally,  $D$  and  $G$  engage in the following two-player minimax game with the value function  $V(G, D)$ :

$$\min_G \max_D V(D, G) = \mathbb{E}_{x \sim p_X(x)}[\log D(x)] + \mathbb{E}_{z \sim p_Z(z)}[\log(1 - D(G(z)))] \quad (3.10)$$

We can see a graphical representation of the GAN framework in Figure 3.6.

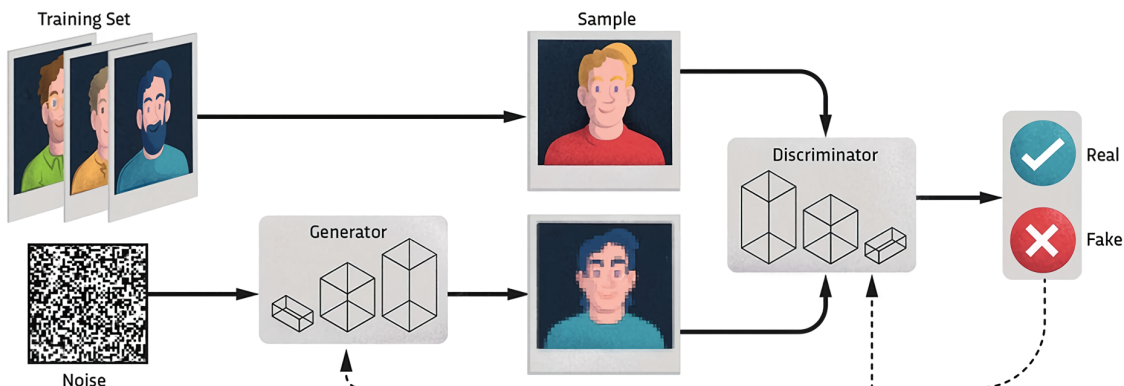


Figure 3.6: GAN framework applied to human faces generation task

Source: Yashwant Singh Kaurav

### 3.3.1 Bidirectional GANs

Generative Adversarial Networks (GANs) have the potential to be used for unsupervised learning of rich feature representations across various data distributions. However, an obvious issue arises because the GAN framework inherently lacks an inverse mapping from generated data back to the latent representation. This limitation means that while the generator can map latent samples to generated data, there is no mechanism to map data back to the latent space.

To address this issue, [Donahue et al., 2017] introduced a novel framework called Bidirectional Generative Adversarial Networks (BiGAN). The BiGAN framework, whose architecture is illustrated in Figure 3.7, enhances the standard GAN model (as introduced by [Goodfellow et al., 2014]) by incorporating an **encoder**. This encoder, denoted as  $E : \Omega_X \rightarrow \Omega_Z$ , maps data  $x$  to latent representations  $z$ , complementing the generator  $G$ .

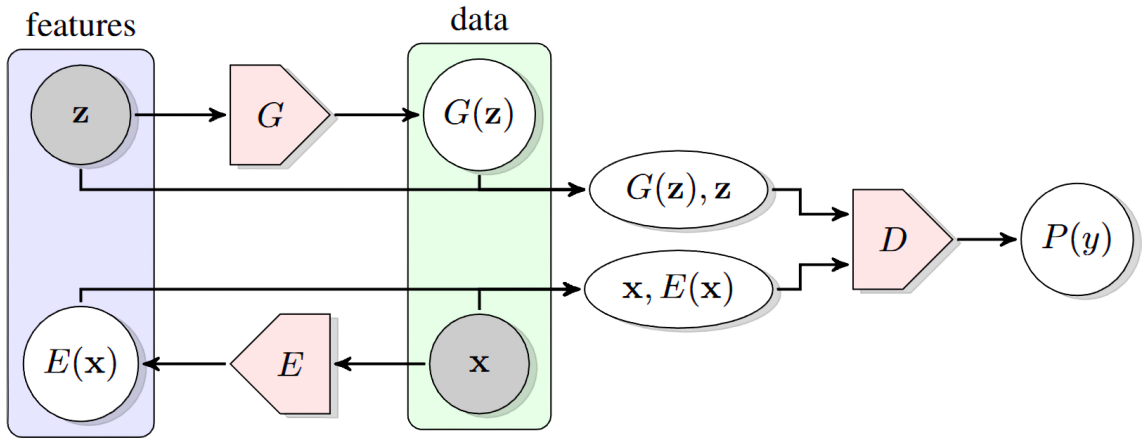


Figure 3.7: BiGAN architecture with generator, discriminator, and encoder.

Source: [Donahue et al., 2017]

In BiGAN, the discriminator  $D$  operates not only in the data space (distinguishing between  $x$  and  $G(z)$ ) but also jointly in the data and latent spaces. Specifically, the discriminator evaluates pairs of data and their corresponding latent representations, distinguishing between real  $(x, E(x))$  and generated  $(G(z), z)$ . Here, the latent component is either an encoder output  $E(x)$  or a generator input  $z$ .

An essential aspect of BiGAN is that the encoder  $E$  is designed to learn an inverse mapping of the generator  $G$ . Despite the encoder and generator not directly interacting, since  $E(G(z))$  is not explicitly computed and the generator does not use  $E(x)$ , the framework ensures that the encoder effectively inverts the generator's mapping.

The training objective for BiGANs is formulated as a minimax problem involving the generator  $G$ , the encoder  $E$ , and the discriminator  $D$ . This objective can be written as:

$$\min_{G,E} \max_D V(D, E, G)$$

where the value function  $V(D, E, G)$  is defined as:

$$V(D, E, G) := \mathbb{E}_{x \sim p_X} [\underbrace{\mathbb{E}_{z \sim p_E(\cdot|x)} [\log D(x, z)]}_{\log D(x, E(x))}] + \mathbb{E}_{z \sim p_Z} [\underbrace{\mathbb{E}_{x \sim p_G(\cdot|z)} [\log(1 - D(x, z))]}_{\log(1 - D(G(z), z))}]. \quad (3.11)$$

In simpler terms, this objective consists of two components:

1. The expectation over the data distribution  $p_X$  and the encoder's latent space distribution  $p_E(\cdot|x)$ , which aims to maximize  $\log D(x, E(x))$ .
2. The expectation over the prior distribution  $p_Z$  and the generator's data distribution  $p_G(\cdot|z)$ , which aims to maximize  $\log(1 - D(G(z), z))$ .

The optimization of this minimax objective is performed using an alternating gradient-based approach, similar to the method introduced by [Goodfellow et al., 2014] for GANs.

### 3.3.2 Bidirectional Conditional GANs

Conditional GAN (cGAN) ([Mirza and Osindero, 2014]) is a variant of standard GANs designed to enable the conditional generation of data samples based on both latent variables (intrinsic factors) and known auxiliary information (extrinsic factors) such as class labels or associated data from other modalities. However, cGANs fails to achieve several key properties:

1. The ability to disentangle intrinsic and extrinsic factors during the generation process.
2. The ability to separate the components of extrinsic factors from each other, ensuring that the inclusion of one factor minimally impacts the others.

[Jaiswal et al., 2018] introduced the Bidirectional Conditional GAN (BiCoGAN). BiCoGAN enhances the cGAN framework by simultaneously training an encoder along with the generator and discriminator. This encoder learns inverse mappings of data samples to both intrinsic and extrinsic factors, thereby overcoming deficiencies in prior approaches. In Figure 3.8, we present the architecture of BiCoGAN.

In the BiCoGAN framework, the generator  $G(\tilde{z}; \theta_G)$  learns a mapping from the distribution  $p_{\tilde{Z}}$ , where  $\tilde{z} = [z, c]$ , to  $p_G$ , with the goal of making  $p_G$  approximate  $p_X$ . Concurrently, the encoder  $E(x; \theta_E)$  learns a mapping from  $p_X$  to  $p_E$ , aiming to make  $p_E$  approximate  $p_{\tilde{Z}}$ . The discriminator  $D$  evaluates real or fake decisions using pairs  $(\tilde{z}, G(\tilde{z}); \theta_D)$  and  $(E(x), x; \theta_D)$ .

The encoder in BiCoGAN must effectively learn the inverse mapping from data  $x$  to latent variables  $z$  and conditions  $c$ , just as the generator must incorporate both to produce data samples that can deceive the discriminator. This requirement follows from the invertibility under the optimality theorem of BiGANs. However,

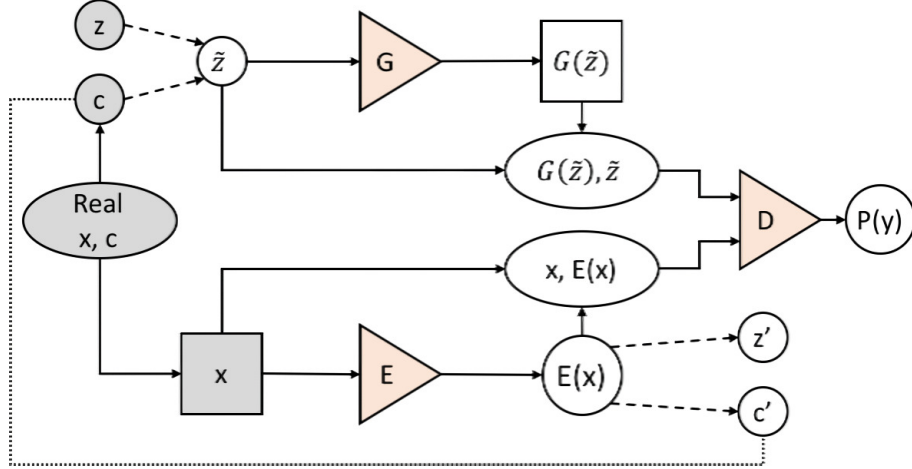


Figure 3.8: BiCoGAN architecture with generator, discriminator, and encoder.

Source: [Jaiswal et al., 2018]

achieving this optimality is challenging in practice, especially when the prior vector contains structured or complex information. While intrinsic factors  $z$  are sampled from a simple latent distribution, extrinsic factors  $c$ , such as class labels or object attributes, have specialized and complex distributions that are more difficult to model.

To address this challenge, we introduce the **extrinsic factor loss** (EFL) as a mechanism to guide BiCoGANs in better encoding extrinsic factors. During training, the condition  $c$  associated with each real data sample is known and can be used to improve the learning of inverse mappings from  $x$  to  $c$ . The specific form of EFL depends on the nature of  $c$  and the dataset or domain in question.

The BiCoGAN value function can be expressed as:

$$\begin{aligned} V(D, G, E) := & \mathbb{E}_{x \sim p_X(x)} [\log D(E(x), x)] \\ & + \gamma \mathbb{E}_{(x, c) \sim p_X(x, c)} [\text{EFL}(c, E_c(x))] \\ & + \mathbb{E}_{z \sim p_{\tilde{Z}}(\tilde{z})} [\log(1 - D(\tilde{z}, G(\tilde{z})))] \end{aligned} \quad (3.12)$$

where  $\gamma$  is the **extrinsic factor loss weight** (EFLW), defined as:

$$\gamma = \min(\alpha e^{\rho t}, \phi)$$

Here,  $\alpha$  is the initial value of  $\gamma$ ,  $\phi$  is its maximum value,  $\rho$  controls the rate of exponential increase, and  $t$  indicates the number of epochs the model has been trained.

### 3.3.3 Wasserstein GANs

In a Generative Adversarial Network (GAN), the interaction between the generator  $G$  and the discriminator  $D$  is formalized as a minimax optimization problem:

$$\min_G \max_D \mathbb{E}_{x \sim p_X} [\log(D(x))] + \mathbb{E}_{\tilde{x} \sim p_G} [\log(1 - D(\tilde{x}))], \quad (3.13)$$

where  $p_X$  represents the real data distribution, and  $p_G$  represents the model distribution implicitly defined by  $\tilde{x} = G(z)$ , with  $z \sim p(z)$ . If the discriminator is optimally trained before each update of the generator's parameters, minimizing this objective corresponds to minimizing the Jensen-Shannon divergence between  $p_X$  and  $p_G$ . However, this often leads to vanishing gradients as the discriminator saturates.

An alternative approach involves using the **Earth-Mover distance** (also known as the Wasserstein-1 distance),  $W(q, p)$ , which measures the minimum cost of transporting mass to transform distribution  $q$  into distribution  $p$ . Under mild assumptions,  $W(q, p)$  is continuous and differentiable almost everywhere.

The **Wasserstein GAN** (WGAN) ([Gulrajani et al., 2017]) modifies the value function using the Kantorovich-Rubinstein duality:

$$\min_G \max_{D \in \mathcal{D}} \mathbb{E}_{x \sim p_X}[D(x)] - \mathbb{E}_{\tilde{x} \sim p_G}[D(\tilde{x})],$$

where  $\mathcal{D}$  is the set of 1-Lipschitz functions, and  $p_G$  is again the model distribution defined by  $\tilde{x} = G(z)$ , with  $z \sim p(z)$ . When the discriminator (referred to as the **critic** in this context) is optimal, minimizing the value function with respect to the generator's parameters minimizes  $W(p_X, p_G)$ .

The WGAN value function leads to a critic function with more well-behaved gradients with respect to its input, facilitating easier optimization of the generator. Empirically, the WGAN value function has been observed to correlate better with sample quality compared to the traditional GAN value function.

To enforce the Lipschitz constraint on the critic, a **gradient penalty** is used. A differentiable function is 1-Lipschitz if its gradients have a norm of at most 1 everywhere. Therefore, the gradient norm of the critic's output with respect to its input is directly constrained. The new objective is:

$$L = \mathbb{E}_{\tilde{x} \sim p_G}[D(\tilde{x})] - \mathbb{E}_{x \sim p_X}[D(x)] + \lambda \mathbb{E}_{\hat{x} \sim p_{\hat{X}}}[(\|\nabla_{\hat{x}} D(\hat{x})\|_2 - 1)^2],$$

where the first two terms represent the original critic loss and the third term is the gradient penalty.

## 3.4 Causal Inference

The **causal inference** is a discipline that studies the relationships of cause-and-effect between variables. Specifically, it is concerned with inferring the causes of an observed phenomenon, distinguishing between **correlation** and **causality**. We are going to explore the basic concepts of causal inference as described in [Neal, 2020].

### 3.4.1 Correlation does not imply Causation

Consider the following scenario: you come across some data showing a correlation between wearing shoes to bed and waking up with a headache. It appears that most people who wear shoes to bed tend to wake up with a headache, while those who

don't wear shoes to bed typically do not wake up with a headache. It is common for people to interpret such data, where there is an **association**, as indicating that wearing shoes to bed causes headaches. This is especially true if they are seeking a reason to avoid wearing shoes to bed.

We can explain the association between wearing shoes to bed and waking up with a headache without implying that one causes the other. Both events are actually caused by a **common factor**: drinking the night before. This relationship is depicted in Figure 3.9.

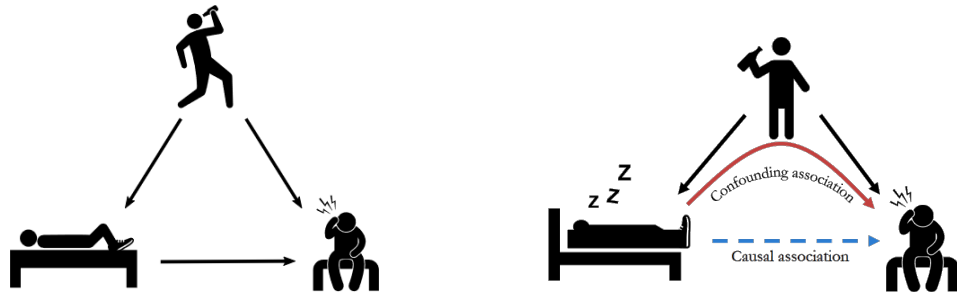


Figure 3.9: A confounding variable causes both wearing shoes to bed and waking up with a headache.

Source: [Neal, 2020]

This kind of variable is often referred to as a **confounder** and we refer to this type of association as a **confounding association** since the observed relationship is influenced by a confounder.

### 3.4.2 The Flow of Association and Causation in Graphs

In the context of modeling associations between variables, we utilize Directed Acyclic Graphs (DAGs). The following assumptions are pertinent to this modeling approach:

- **Minimality Assumption:** composed of:
  - **Local Markov Assumption (LMA):** Each node is conditionally independent of its non-descendants given its parents.
  - **Dependency of Adjacent Nodes:** Nodes that are adjacent in the DAG are dependent.
- **Bayesian Network Factorization (BNF):** The joint probability distribution can be factorized as

$$P(x_1, \dots, x_n) = \prod_i P(x_i | \text{pa}_i) \quad (3.14)$$

where  $\text{pa}_i$  denotes the parents of node  $x_i$ . If  $P$  factorizes  $G$ , then  $P$  is Markovian with respect to  $G$ , in fact the Local Markov Assumption is valid if and only if the Bayesian Network Factorization is also valid.

- **Causal Edges Assumption:** In a DAG, every parent is a direct cause of all its children.

But what is a **cause**? A variable  $X$  is said to be a cause of a variable  $Y$  if  $X$  can change in response to changes in  $Y$ .

In Figure 3.10, we can see how implementing each one of these assumptions leads to having different relationships between the variables in the graph.

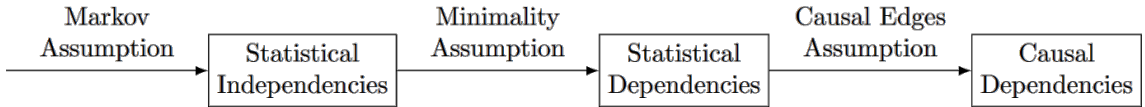


Figure 3.10: Different relationships between variables in a graph based on the assumptions.

Source: [Neal, 2020]

This brings us to the core of this section: understanding the flow of association and causation in DAGs. We can comprehend this flow in general DAGs by analyzing the minimal building blocks of graphs.

By **flow of association**, we mean whether any two nodes in a graph are associated or not associated. In other words, whether two nodes are (statistically) dependent or (statistically) independent. Additionally, we will explore whether two nodes are conditionally independent or not.

Consider a graph consisting of just two unconnected nodes, as depicted in Figure 3.11.



Figure 3.11: Graph with two unassociated nodes.

These nodes are not associated simply because there is no edge between them. This can be demonstrated by considering the factorization of  $P(x_1, x_2)$  given by the Bayesian Network Factorization:

$$P(x_1, x_2) = P(x_1)P(x_2)$$

This factorization immediately proves that the two nodes  $X_1$  and  $X_2$  are unassociated (independent) in this basic structure. The key assumption here is that  $P$  is Markov with respect to the graph in Figure 3.11.

In contrast, if there is an edge between the two nodes (as in Figure 3.12), then the nodes are associated. The assumption used here is the causal edges assumption, which indicates that  $X_1$  is a cause of  $X_2$ . Since  $X_1$  is a cause of  $X_2$ ,  $X_2$  must be able to change in response to changes in  $X_1$ , establishing their association. Generally, any time two nodes are adjacent in a causal graph, they are associated.

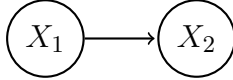


Figure 3.12: Graph with two nodes  $X_1$  and  $X_2$  with an arrow from  $X_1$  to  $X_2$ , indicating that  $X_1$  is a cause of  $X_2$ .

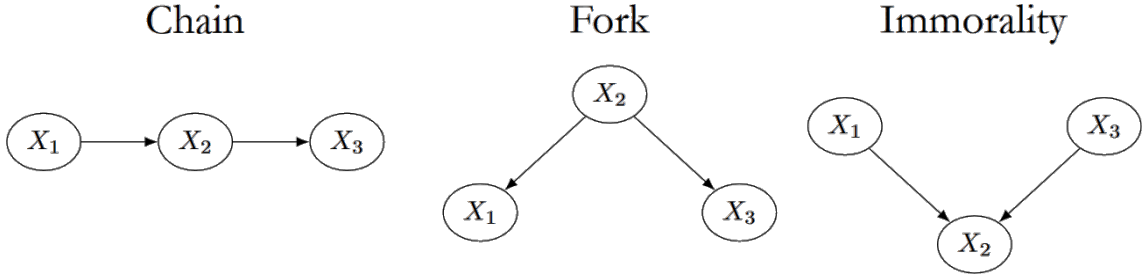


Figure 3.13: Building blocks of DAGs: chain, fork, and immorality.

Source: [Neal, 2020]

Let's now consider more the building blocks of DAGs as shown in Figure 3.13, where we have a **chain**, a **fork** and an **immorality**.

Chains and forks share the same set of dependencies. In both structures,  $X_1$  and  $X_2$  are dependent, and  $X_2$  and  $X_3$  are dependent for the same reason discussed for the graph in Figure 3.12. Adjacent nodes are always dependent when we make the causal edges assumption. But does association flow from  $X_1$  to  $X_3$  through  $X_2$  in chains and forks?

In chain graphs,  $X_1$  and  $X_3$  are usually dependent simply because  $X_1$  causes changes in  $X_2$ , which then causes changes in  $X_3$ . In a fork graph,  $X_1$  and  $X_3$  are also usually dependent because the value that  $X_2$  takes on determines both the value that  $X_1$  takes on and the value that  $X_3$  takes on. In other words,  $X_1$  and  $X_3$  are associated through their shared common cause. However, while in chains the association between  $X_1$  and  $X_3$  is a causal one, in forks it is not.

Chains and forks also share the same set of independencies. When we condition on  $X_2$  in both graphs, it blocks the flow of association from  $X_1$  to  $X_3$ . This is due to the local Markov assumption; each variable can locally depend only on its parents. Therefore, when we condition on  $X_2$  (the parent of  $X_3$  in both graphs),  $X_3$  becomes independent of  $X_1$  (and vice versa).

We refer to this independence as an instance of a blocked path. These blocked paths are illustrated in Figure 3.14.

In contrast to chains and forks, in an immorality,  $X_1 \perp X_3$ . We observe that conditioning on a collider can turn a blocked path into an unblocked path. The parents  $X_1$  and  $X_3$  are not associated in the general population, but when we condition on their shared child  $X_2$  taking on a specific value, they become associated. Conditioning on the collider  $X_2$  allows association to flow along the path  $X_1 \rightarrow X_2 \leftarrow X_3$ , despite the fact that it does not when we do not condition on  $X_2$ . In Figure 3.15, we can see the immorality with the blocked path and the unblocked path.

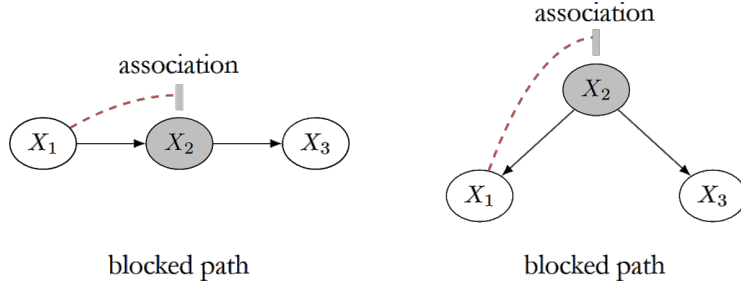


Figure 3.14: Blocked paths in chain and fork graphs.

Source: [Neal, 2020]

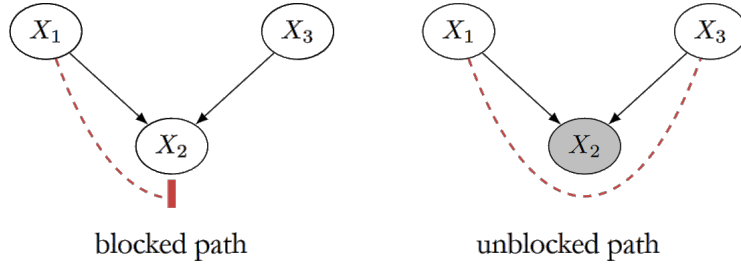


Figure 3.15: Immorality with a blocked path and an unblocked path.

Source: [Neal, 2020]

Conditioning on **descendants of a collider** also induces association between the parents of the collider. The intuition is that if we learn something about a collider's descendant, we usually also learn something about the collider itself because there is a direct causal path from the collider to its descendants. In Figure 3.16, we can see a conditioning on a descendant of a collider.

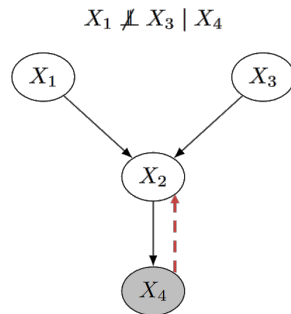


Figure 3.16: Conditioning on a descendant of a collider.

Source: [Neal, 2020]

Now let's formally codify the concept of a **blocked path**: a path between nodes \$X\$ and \$Y\$ is **blocked** by a (potentially empty) conditioning set \$Z\$ if either of the following is true:

1. Along the path, there is a chain \$\dots \rightarrow W \rightarrow \dots\$ or a fork \$\dots \leftarrow W \rightarrow \dots\$, where \$W\$ is conditioned on (\$W \in Z\$).

2. There is a **collider**  $W$  on the path that is not conditioned on ( $W \notin Z$ ) and none of its descendants are conditioned on ( $de(W) \not\subseteq Z$ ).

An **unblocked path** is simply a path that is not blocked. The graphical intuition to have in mind is that **association** flows along unblocked paths and does not flow along blocked paths.

Now, we are ready to introduce **d-separation**: two (sets of) nodes  $X$  and  $Y$  are **d-separated** by a set of nodes  $Z$  if all of the paths between (any node in)  $X$  and (any node in)  $Y$  are blocked by  $Z$  ([Pearl, 1988]).

Otherwise, they are **d-connected**.

### 3.4.3 Potential Outcomes and the Fundamental Problem of Causal Inference

The central issue driving the need for causal inference is that correlation does not imply causation. If these two concepts were equivalent, causal inference would be easy. This raises the critical question: how can we determine when one event causes another and, therefore, infer causality?

To address this, we introduce the concept of **potential outcomes**. Suppose, as shown in Figure 3.17, you have a headache, and you know that taking a pill would alleviate the headache, whereas not taking the pill would result in the headache persisting. In this scenario, you can infer a causal effect of the pill on the headache. However, if not taking the pill also resulted in the headache disappearing, you would conclude that there is no causal effect. This is the intuition behind potential outcomes.

Let's define some notation:

- $T$ : Observed treatment
- $Y$ : Observed outcome
- $i$ : Denotes a specific unit or individual
- $Y_i|_{do(T=1)} \triangleq Y_i(1)$ : Potential outcome under treatment
- $Y_i|_{do(T=0)} \triangleq Y_i(0)$ : Potential outcome under no treatment
- **Causal Effect** =  $Y_i(1) - Y_i(0)$

To account for individual differences, we measure the **Average Treatment Effect** (ATE), given by:

$$\mathbb{E}[Y(1)] - \mathbb{E}[Y(0)]. \quad (3.15)$$

A fundamental problem in causal inference is the challenge of distinguishing between the observational distribution  $P(Y|T = t)$  and the interventional distribution  $P(Y|do(T = t))$ . These distributions are generally not equal; if they were, correlation would indeed imply causation. The intervention  $T = t$  on a population is

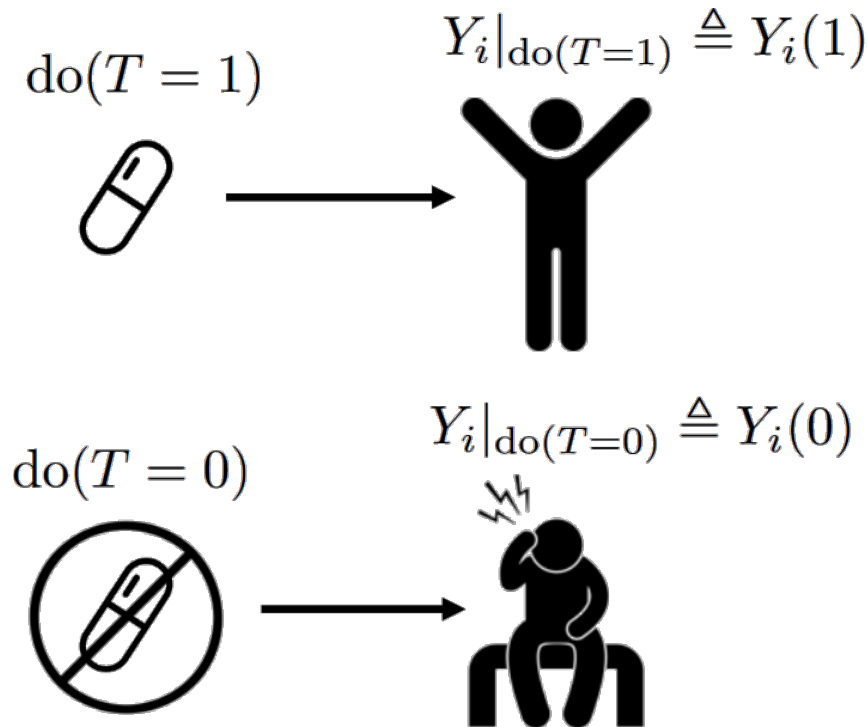


Figure 3.17: Potential outcomes for a causal effect.

Source: [Neal, 2020]

denoted by the do-operator, which allows us to measure the causal effect from the interventional distribution  $P(Y|\text{do}(T = t))$ .

However, we often cannot intervene on the entire population and can only access the observational distribution. The distinction between these distributions is illustrated in Figure 3.18. Intervening with  $\text{do}(T = 0)$  (**factual**) usually precludes access to  $\text{do}(T = 1)$  (**counterfactual**).

One approach to address this issue is through a **Randomized Controlled Trial** (RCT). In an RCT, participants are randomly assigned to treatment or control groups, ensuring that  $(Y(1), Y(0)) \perp\!\!\!\perp T$ , under the assumption of exchangeability. **Exchangeability** means that the treatment groups are comparable in the sense that if they were swapped, the new treatment group would exhibit the same outcomes as the original treatment group, and the new control group would exhibit the same outcomes as the original control group. The randomization process ensures that, as we can see in Figure 3.19, the causal association between the treatment and the outcome is identifiable since there is no confounding due to a missing connection between the treatment and the cause.

However, it is not always feasible to randomize treatment due to several reasons:

- **Ethical reasons:** For instance, it would be unethical to randomize people to smoke in order to measure the effect on lung cancer.
- **Infeasibility:** It is impractical to randomize countries into different economic systems (e.g. communist vs. capitalist) to measure the effect on GDP.

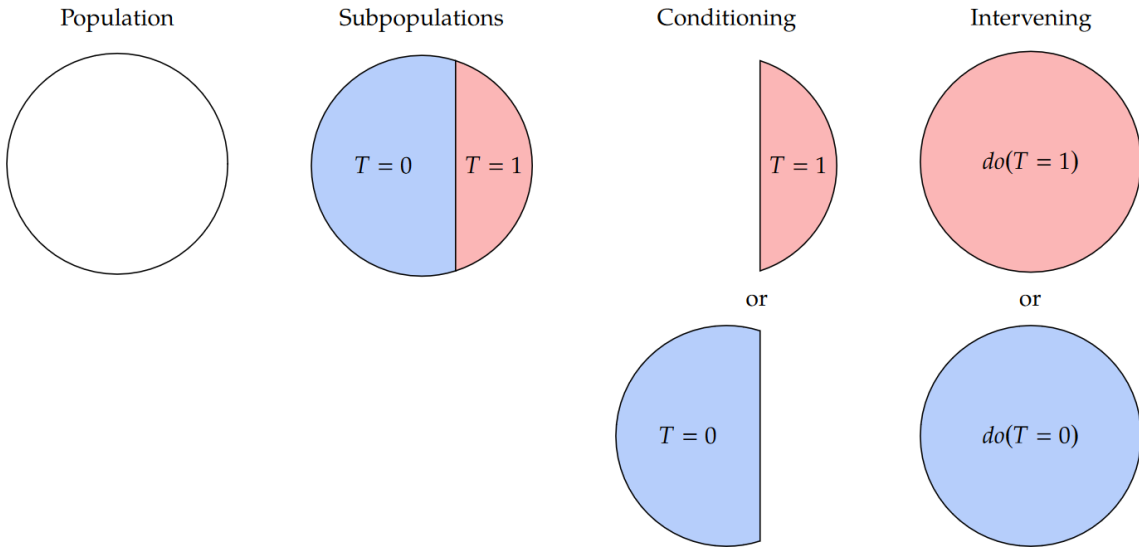


Figure 3.18: The difference between observational and interventional distributions.

Source: [Neal, 2020]

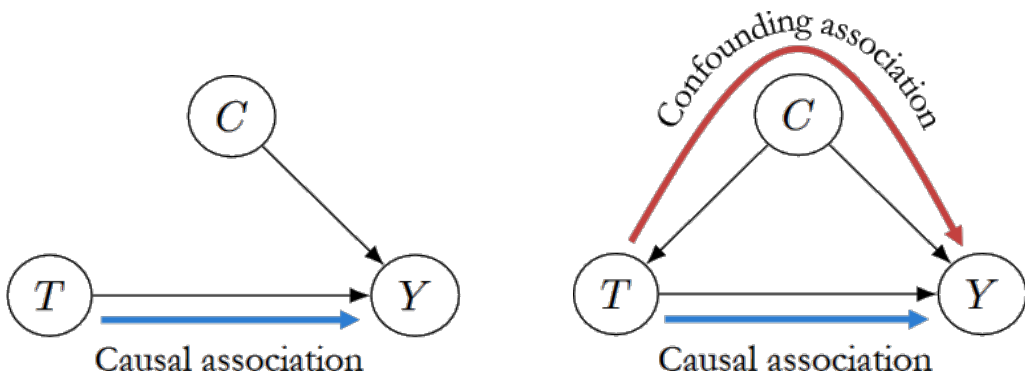


Figure 3.19: Randomized Controlled Trial (RCT) design vs. Observational Study.

Source: [Neal, 2020]

- **Impossibility:** Certain changes, such as altering a person's DNA at birth to measure the effect on breast cancer, are simply not possible.

We must then find a way to estimate causal effects from observational data.

#### 3.4.4 Causal Models and Identification

**Identification** is the process of moving from a **causal estimand** to a **statistical estimand**. As we have seen in 3.4.3, conditioning on  $T = t$  means that we are restricting our focus to the subset of the population who received treatment  $t$ . In contrast, an **intervention** (denoted with the **do-operator**) involves taking the entire population and giving everyone treatment  $t$ .

**Interventional distributions** such as  $P(Y | do(T = t))$  are conceptually quite different from the **observational distribution**  $P(Y)$  since the latter do not include the do-operator. Because of this, we can observe data from them without conducting

any experiments. This is why we call data from  $P(Y, T, X)$  **observational data**. If we can reduce an expression  $Q$  with  $\text{do}$  in it (an interventional expression) to one without  $\text{do}$  in it (an observational expression), then  $Q$  is said to be **identifiable**. We will refer to an estimand as a **causal estimand** when it contains a  $\text{do}$ -operator, and as a **statistical estimand** when it does not contain a  $\text{do}$ -operator.

Before describing a very important assumption, we must specify what a **causal mechanism** is, we will refer to the causal mechanism that generates  $X_i$  as the conditional distribution of  $X_i$  given all of its causes:  $P(x_i | \text{pa}_i)$ .

To achieve many causal identification results, the main assumption we will make is that interventions are local: intervening on a variable  $X_i$  only changes the causal mechanism for  $X_i$ . In this sense, the causal mechanisms are **modular**.

**Assumption of Modularity / Independent Mechanisms / Invariance:** If we intervene on a set of nodes  $S \subseteq [n]$ <sup>1</sup>, setting them to constants, then for all  $i$ , we have the following:

1. If  $i \notin S$ , then  $P(x_i | \text{pa}_i)$  remains unchanged.
2. If  $i \in S$ , then  $P(x_i | \text{pa}_i) = 1$  if  $x_i$  is the value that  $X_i$  was set to by the intervention; otherwise,  $P(x_i | \text{pa}_i) = 0$ .

The modularity assumption allows us to encode many different interventional distributions in a single graph. For example, it could be the case that  $P(Y)$ ,  $P(Y | \text{do}(T = t))$ ,  $P(Y | \text{do}(T = t'))$ , and  $P(Y | \text{do}(T_2 = t_2))$  are all completely different distributions that share almost nothing. If this were the case, each of these distributions would need its own graph. However, by assuming modularity, we can encode them all with the same graph that we use to encode the joint  $P(Y, T, T_2, \dots)$ , and we can know that all of the factors (except the ones that are intervened on) are shared across these graphs.

The **causal graph** for interventional distributions, as shown in an example in Figure 3.20, is simply the same graph used for the observational joint distribution, but with all of the edges to the intervened node(s) removed. This is because the probability for the intervened factor has been set to 1, allowing us to ignore that factor.

Recall from subsection 3.4.2, that **causal association** flows from  $T$  to  $Y$  along directed paths, while **non-causal association** can flow along other paths from  $T$  to  $Y$  unless they are blocked by either a non-collider that is conditioned on or a collider that is not conditioned on. These non-directed unblocked paths from  $T$  to  $Y$  are known as **backdoor paths** because they have an edge that goes in the “backdoor” of the  $T$  node. By conditioning on certain variables, we can block these paths and identify causal quantities like  $P(Y | \text{do}(T = t))$ .

Our goal is to transform the causal estimand  $P(y | \text{do}(T = t))$  into a statistical estimand that relies only on the observational distribution. We start by assuming we have a set of variables  $W$  that satisfy the **backdoor criterion**:

---

<sup>1</sup>We use  $[n]$  to refer to the set  $\{1, 2, \dots, n\}$ .

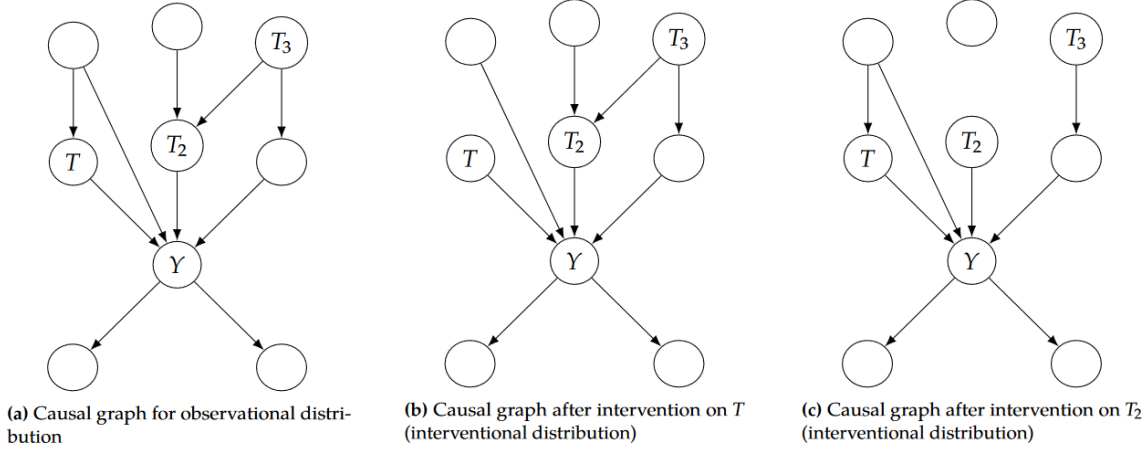


Figure 3.20: Intervention as edge deletion in causal graphs.

Source: [Neal, 2020]

A set of variables  $W$  satisfies the backdoor criterion relative to  $T$  and  $Y$  if the following are true:

1.  $W$  blocks all backdoor paths from  $T$  to  $Y$ .
2.  $W$  does not contain any descendants of  $T$ .

When  $W$  satisfies the backdoor criterion, it becomes a **sufficient adjustment set**. Additionally, we must ensure **positivity**, which means that all subgroups of the data with different covariates have some probability of receiving any value of treatment. Formally, we define **positivity** for binary treatment as follows:

For all values of covariates  $x$  present in the population of interest (i.e.,  $x$  such that  $P(X = x) > 0$ ),

$$0 < P(T = 1 \mid X = x) < 1$$

**Backdoor Adjustment:** Given the modularity assumption, that  $W$  satisfies the backdoor criterion, and positivity, we can identify the causal effect of  $T$  on  $Y$ :

$$P(y \mid \text{do}(T = t)) = \sum_w P(y \mid T = t, W = w)P(w) \quad (3.16)$$

This theorem connects to **d-separation**. We can use the backdoor adjustment if  $W$  **d-separates**  $T$  from  $Y$  in the manipulated graph. Recall that isolating the causal association means identifying it. We achieve this if  $T$  is d-separated from  $Y$  in the manipulated graph or if  $Y$  is d-separated from  $T$  in the manipulated graph, conditional on  $W$ . In Figure 3.21, we can see how the backdoor paths that are blocked by conditioning on  $W$  allow us to identify the causal effect of  $T$  on  $Y$ .

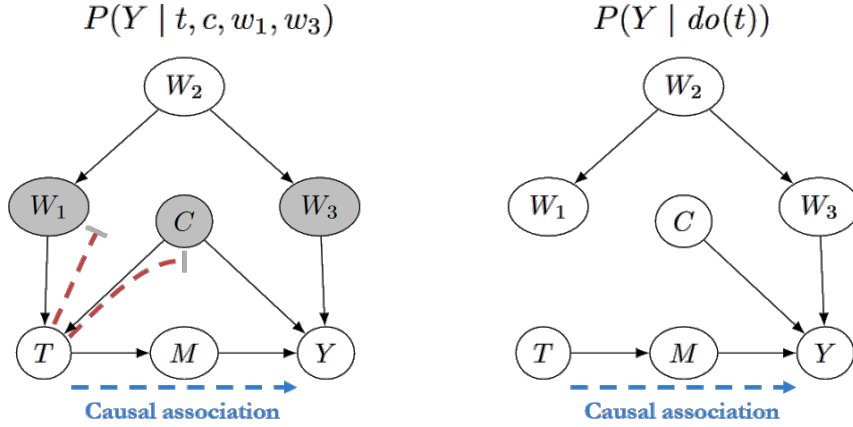


Figure 3.21: Backdoor paths blocked by conditioning on  $W$ .

Source: [Neal, 2020]

### 3.4.5 Structural Causal Models

We need to be able to state that  $A$  is a **cause** of  $B$ , meaning that changing  $A$  results in changes in  $B$ , but changing  $B$  does not result in changes in  $A$ . This relationship is represented by the following **structural equation**:

$$B := f(A) \quad (3.17)$$

where  $f$  is some function that maps  $A$  to  $B$ .

However, the mapping between  $A$  and  $B$  in Equation 3.17 is **deterministic**. Ideally, we'd like to allow it to be **probabilistic**, which allows room for some unknown causes of  $B$  that factor into this mapping. We can then write the following:

$$B := f(A, U) \quad (3.18)$$

where  $U$  is some unobserved random variable. The graph for this simple structural equation is shown in Figure 3.22.

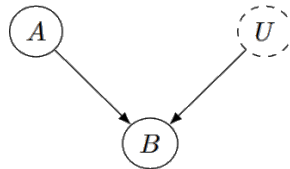


Figure 3.22: Graph of 3.18. The dashed node  $U$  means that  $U$  is unobserved.

Source: [Neal, 2020]

While we have shown a single **structural equation** in Equation 3.18, there can be a large collection of structural equations in a single model, commonly labeled  $M$ . For example, we write structural equations for the causal model in Figure 3.23

below:

$$M : \begin{cases} B := f_B(A, U_B) \\ C := f_C(A, B, U_C) \\ D := f_D(A, C, U_D) \end{cases} \quad (3.19)$$

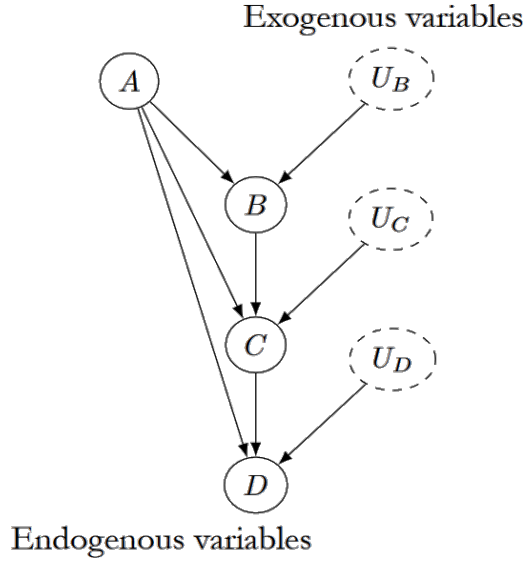


Figure 3.23: Graph of 3.19.

Source: [Neal, 2020]

The variables for which we write structural equations are known as **endogenous variables**. These are the variables whose causal mechanisms we are modeling. In contrast, **exogenous variables** are variables that do not have any parents in the causal graph.

**Structural Causal Model (SCM):** a structural causal model is a tuple consisting of the following sets:

1. A set of endogenous variables  $V$
2. A set of exogenous variables  $U$
3. A set of functions  $f$ , one to generate each endogenous variable as a function of other variables

## Chapter 4

# Methodology

## 4.1 Problem Statement

In this work, we address the challenge of training an agent using an offline Deep Reinforcement Learning (DRL) algorithm with access to a pre-collected dataset  $\mathcal{D}$  of experiences. Each experience in  $\mathcal{D}$  captures an interaction with the environment and is represented as a tuple

$$T = (s_t, s_{t+1}, a_t, r_{t+1}).$$

Here,  $s_t$  and  $s_{t+1}$  are the **observed states** at time-steps  $t$  and  $t+1$ , respectively,  $a_t$  is the **action** taken at time  $t$ , and  $r_{t+1}$  is the **reward** received after taking action  $a_t$  and transitioning to state  $s_{t+1}$ . States can be represented in various forms:

- **Numerical data:** consisting of a stack of vectors of real numbers representing the physical state of the environment (e.g., position, velocity, orientation in robotics, suffering from anemia or not in healthcare).
- **Images:** consisting of a sequence of images observed by the agent (e.g., frames from a camera mounted on a robot or a patient's medical images).
- **Images and numerical data:** a combination of the above two representations (e.g., images from a robot's camera and its joint angles).

The number of images (or vectors) in the state representation is denoted by  $N_S$  such that

$$s_t = \{\mathcal{S}_{t-(N_S-1)}, \dots, \mathcal{S}_{t-1}, \mathcal{S}_t\} \text{ and } s_{t+1} = \{\mathcal{S}_{t-(N_S-2)}, \dots, \mathcal{S}_t, \mathcal{S}_{t+1}\}$$

where  $\mathcal{S}_t = \{\text{'num': } \mathcal{X}_t, \text{'img': } \mathcal{I}_t\}$  or  $\mathcal{S}_t = \{\text{'num': } \mathcal{X}_t\}$  or  $\mathcal{S}_t = \{\text{'img': } \mathcal{I}_t\}$ .

In real-world scenarios, where comprehensive simulators are unavailable, the dataset  $\mathcal{D}$  may lack experience due to potential risks (e.g., collisions, patient harm) or high costs. This deficiency can prevent the agent's training and result in policies that are neither effective nor robust. Therefore, our goal is to **augment**  $\mathcal{D}$  by generating additional experiences that **align with the environment's underlying transition dynamics**.

To model these state-transition dynamics, we use a **Structural Causal Model** (SCM) defined as:

$$S_{t+1} = f_s(S_t, A_t, U_{t+1})$$

where  $S_{t+1}$ ,  $S_t$ , and  $A_t$  are random variables representing the states and action, while  $U_{t+1}$  represents unobserved variables affecting the transition. The function  $f_s$  captures the causal mechanism determining the next state  $S_{t+1}$  from its causes  $S_t$ ,  $A_t$ , and  $U_{t+1}$ . Additionally, we model the reward as:

$$R_{t+1} = f_r(S_t, S_{t+1}, A_t)$$

If  $f_s$  and  $f_r$  are known, we can generate **counterfactual** experiences.

Given an observed tuple  $T = (s_t, s_{t+1}, a_t, r_{t+1})$ , we aim to create a new tuple  $T' = (s_t, s'_{t+1}, a'_t, r'_{t+1})$  representing what might have occurred if a different action  $a'_t$  were taken in state  $s_t$ . This involves the following steps:

1. **Abduction:** Estimate  $U_{t+1} = \hat{u}_{t+1}$  from the observed data  $T = (s_t, s_{t+1}, a_t, r_{t+1})$ ;
2. **Action:** Perform the counterfactual action  $a'_t \neq a_t$ ;
3. **Prediction:** Use the estimated  $\hat{u}_{t+1}$  and the updated SCM model to predict  $s'_{t+1}$  and  $r'_{t+1}$ .

A key question in counterfactual reasoning is whether the counterfactual outcome is identifiable given the observed data. The following theorem, presented in [Lu et al., 2020], shows that under weak assumptions, the counterfactual outcome is indeed identifiable.

**Theorem 4.1.1.** *Suppose the state transition  $S_{t+1}$  satisfies the following SCM:*

$$S_{t+1} = f_s(S_t, A_t, U_{t+1})$$

*where  $U_{t+1} \perp\!\!\!\perp (S_t, A_t)$ , and the function  $f_s$  is smooth and strictly monotonic in  $U_{t+1}$  for fixed values of  $S_t$  and  $A_t$ . Suppose we have observed  $\langle S_t = s_t, A_t = a, S_{t+1} = s_{t+1} \rangle$ , then the counterfactual outcome for the counterfactual action  $A_t = a'$ :*

$$S_{t+1, A_t=a'} | S_t = s_t, A_t = a, S_{t+1} = s_{t+1}$$

*is identifiable.*

The strict monotonicity of  $f$  in  $U_{t+1}$  guarantees that the unobserved noise term  $U_{t+1}$  can be recovered from the observed  $\langle S_t, A_t, S_{t+1} \rangle$ . With the recovered  $U_{t+1}$ , we can then predict the counterfactual outcome  $S_{t+1, A_t=a'}$  by plugging in the new action  $a'$  into the SCM.

This theorem holds regardless of whether the state and action spaces are continuous or discrete, and it does not depend on the specific form of  $f_s$  or the distribution of  $U_{t+1}$ , as long as the monotonicity condition is satisfied. The key insight is that the counterfactual outcome is identifiable under weak assumptions, making counterfactual reasoning generally possible in a wide range of models and settings. In experiments, this strict monotonicity can be easily implemented through a monotonic multi-layer perceptron network while we will ensure that  $U_{t+1}$  is, in fact, independent of  $(S_t, A_t)$  in our environments by observing their assumed SCM graph.

By creating these counterfactual samples, we can form an augmented dataset  $\mathcal{D}'$ , which can then be used to train an offline DRL agent.

In practice, however, neither  $f_s$  and  $f_r$ , nor the function to perform the abduction step and estimate the unobserved variable  $U_{t+1}$  are known. In the following, we present the framework we devised to infer the SCM model from the available data  $\mathcal{D}$  and simultaneously learn a function to estimate  $U_{t+1}$  (see Subsection 4.3.1). Additionally, we investigated a method where the noise is known and counterfactual states are collected (see Subsection 4.3.2). This approach shifts the problem towards developing the most accurate and representative simulator.

## 4.2 Simulation Environments

Here we introduce the simulation environments used in our experiments, which are essential for creating the dataset  $\mathcal{D}$  and training the offline DRL agents.

Two categories of environments are considered: **Robotics** and **Healthcare**.

### 4.2.1 Robotics Environments

**MuJoCo** (Multi-Joint dynamics with Contact) is a physics engine developed by [Todorov et al., 2012] that has become a standard tool in reinforcement learning research. It provides a platform for simulating complex multi-joint dynamics and it's widely used in application areas which demand fast and accurate simulation of articulated structures interacting with their environment.

The environments we focus on in this work are **HalfCheetah** and **Ant**, their wrapper can be found, as initially presented in [Brockman et al., 2016], in the OpenAI Gym toolkit. In addition to these, we also include **Acrobot**, a classic control problem also available in the OpenAI Gym toolkit and based on the work of [Sutton and Barto, 1998]. Its inclusion provides a contrast to the more complex MuJoCo environments and allows us to test our methods on a wider range of control problems.

In these robotics environments, we can consider various SCMs to capture the state-transition dynamics. For example:

1.  $S_{t+1} = f_s(S_t, A_t, U_{t+1})$ , where  $U_{t+1}$  is causally dependent on  $U_{t+1}$ ,  $S_{t+1}$  is causally dependent on  $S_t$  and  $A_t$ , and  $A_t$  is causally dependent on  $S_t$ . Shown in Figure 4.1a.
2.  $S_{t+1} = f_s(S_t, A_t, U_{t+1})$ , like on the first case, but the noise terms  $U_{t+i}$  are independent among each other. Shown in Figure 4.1b.
3.  $S_{t+1} = f_s(S_t, A_t, U_{t+1})$ , like on the first case, but  $S_{t+1}$  is causally dependent on both  $S_{t+1}$  and  $S_t$ . Shown in Figure 4.1c.
4.  $S_{t+1} = f_s(S_t, A_t, U_{t+1})$ , like on the third case, but the noise terms  $U_{t+i}$  are independent among each other. Shown in Figure 4.1d.

In all these cases, we can effectively show that  $U_{t+1} \perp\!\!\!\perp (S_t, A_t)$  thanks to the rules of **d-separation** shown in Subsection 3.4.4. In Figure 4.2a, we present a visual representation of the d-separation rules for one of the SCMs considered in this work (these conditions hold for all the SCMs considered): since  $S_{t-1}$ ,  $A_{t-1}$  and  $U_t$  are observed and conditioned upon the flow of association given by their fork structure is blocked, the only way for  $U_t$  to influence  $S_t$  could be through their common child  $S_{t+1}$ , which is unobserved, so the independence condition holds.

A case where the independence condition may not hold would be an SCM of the form:

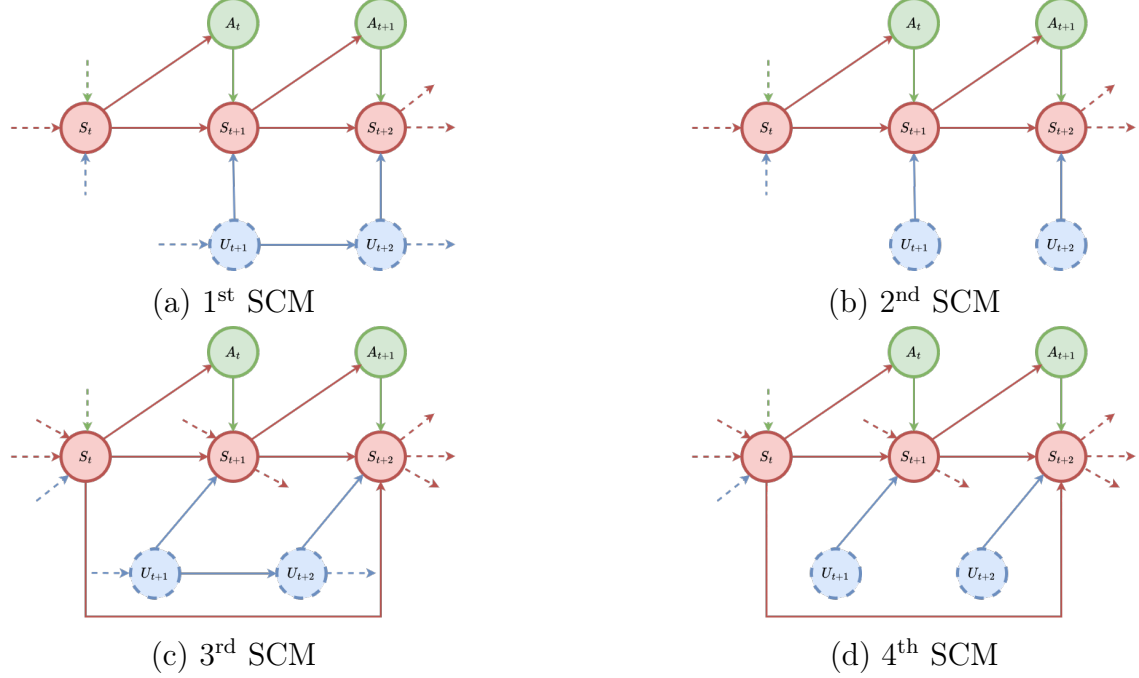


Figure 4.1: SCMs for the robotics environments.

5.  $S_{t+1} = f_s(S_t, A_t, U_{t+1})$ , where the noise term  $U_{t+1}$  depends on the concurrent action  $A_t$ . This scenario, where the action affects the noise at the same time, is a rather difficult condition to achieve in the simulation environments considered in this work. Shown in Figure 4.2b.

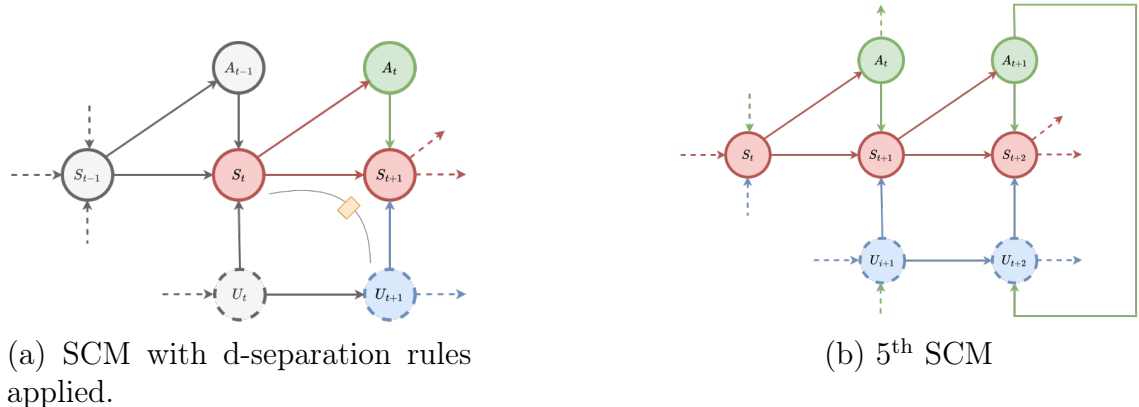


Figure 4.2: SCMs and association rules.

We applied a gaussian noise  $\sim \text{Normal}(\mu = 0.01, \sigma = 1)$  on the state at each timestep in all the robotic environments.

### Acrobot

The Acrobot environment [Farama Org., 2023a] simulates a two-link pendulum with only the second joint actuated. A screenshot of the Acrobot environment is shown in Figure 4.3.

**Description:** The Acrobot system consists of two links connected linearly to form a chain, with one end of the chain fixed and the other end free. The joint between the two links is actuated. The goal is to swing the free end of the chain above the fixed base by applying torques on the actuated joint.

**State space:** The state space consists of 6 continuous variables:

- $\cos(\alpha_t), \sin(\alpha_t), \cos(\beta_t), \sin(\beta_t)$
- Angular velocity of  $\alpha_t$  and  $\beta_t$

The placement of the angles can be seen in Figure 4.3. The angles are measured counterclockwise.

**Action space:** The action space is discrete with 3 possible actions:

1. Apply a negative torque of -1 to the actuated joint
2. Apply no torque (0) to the actuated joint
3. Apply a positive torque of +1 to the actuated joint

**Reward function:** The reward function is defined as:

$$R = -1 \times \text{number of timesteps (with a limit on 100)} \quad (4.1)$$

**Termination conditions:** The episode terminates when either the goal position is reached or the maximum number of timesteps (500) is reached.

### Episode termination

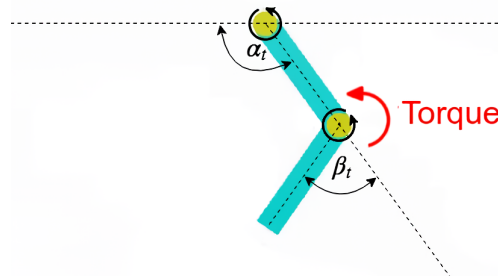


Figure 4.3: Screenshot of the Acrobot environment with information about the state.

Source: [Chevtchenko et al., 2023]

## Half Cheetah

The Half Cheetah environment [Farama Org., 2023c] simulates a 2-dimensional robot with two paws, a screenshot of said environment is shown in Figure 4.4.

**Description:** The Half Cheetah is a 2-dimensional robot composed of 9 body segments connected by 8 joints, including two paws. The objective is to apply torques to these joints to propel the cheetah forward (to the right) as quickly as possible. The torso and head of the cheetah remain fixed and torque can be applied only to the other 6 joints, which include the connections between the torso and the front and back thighs, the thighs and shins, and the shins and feet.

**State space:** The state space consists of positional values of different body parts of the Half Cheetah, followed by the velocities of those individual parts (their derivatives), with all the positions ordered before all the velocities.

**Action space:** The action space consists of 6 continuous values included in  $[-1, 1]$ , corresponding to the torques applied to each one of the joints.

**Reward function:** The reward is typically the **forward** reward - a reward for moving forward, minus the **ctrl** cost - a cost for applying excessively large actions. The reward function is defined as:

$$R = \text{healthy\_reward} + \text{forward\_reward} - \text{ctrl\_cost} \quad (4.2)$$

where

$$\text{ctrl\_cost} = \text{ctrl\_cost\_weight} \times \text{sum}(\text{action}^2) \quad (4.3)$$

and **ctrl\_cost\_weight** is a hyperparameter with a default value of 0.1.

**Termination conditions:** The episode terminates if the Half Cheetah falls over (typically defined as when the torso's z-coordinate falls below a threshold) or if any of the state space values is no longer finite.

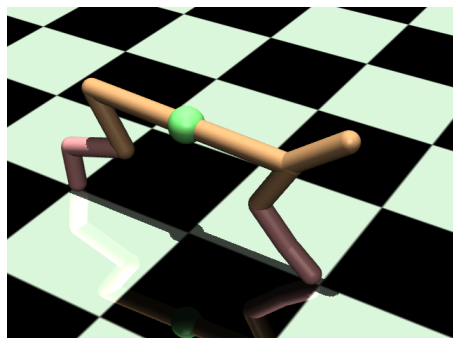


Figure 4.4: Screenshot of the Half Cheetah environment.

Source: [De Lazcano, 2022]

## Ant

The Ant environment [Farama Org., 2023b] simulates a four-legged robot in a plane. A screenshot of the Ant environment is shown in Figure 4.5.

**Description:** The Ant consists of a torso and four legs, each with two joints, resulting in a total of 8 actuated joints. The goal is to coordinate the four legs to move forward (to the right) by applying torques to the eight hinges that connect the nine body parts, consisting of each leg's two segments and the torso.

**State space:** The state space consist of positional values of different body parts of the ant, followed by the velocities of those individual parts (their derivatives) with all the positions ordered before all the velocities.

**Action space:** The action space consists of 8 continuous values included in  $[-1, 1]$ , corresponding to the torques applied to each one of the joints.

**Reward function:** The reward is typically a combination of the **healthy** reward - a fixed reward for each timestep where the ant is alive and the **forward** reward - a reward for moving forward, all this minus the **ctrl** cost - a cost for applying for taking excessively large actions and, eventually, a **contact** cost - a negative reward applied if the external contact force is too large. The reward function is defined as:

$$R = \text{healthy\_reward} + \text{forward\_reward} - \text{ctrl\_cost} [-\text{contact\_cost}] \quad (4.4)$$

**Termination conditions:** The episode terminates if the ant falls over (typically defined as when the torso's z-coordinate falls below a threshold) or if any of the state space values is no longer finite.

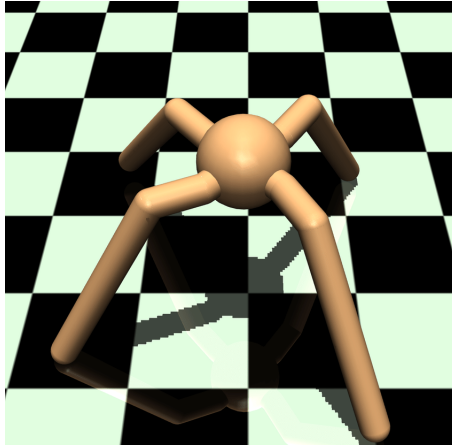


Figure 4.5: Screenshot of the Ant environment.

Source: [Venuto et al., 2020]

### 4.2.2 Healthcare Environments

The only healthcare environment we focus on in this work is the **Diabetes** environment.

#### Diabetes

In our study, we employ a simulated dataset that models the progression of type II diabetes and the effects of antihyperglycaemic drugs, as seen in [Daniel et al., 2013].

This simulation represents a simplified version of a longitudinal medical study with time-varying confounders.

The key features of the simulated dataset:

1. Variables:

- $U_0$ : Binary indicator of subject's health status prior to randomization (unmeasured)
- $A_0, A_1$ : Binary indicators for antglycaemic drug prescription at visits 0 and 1 (actions)
- $L_1$ : Binary indicator for anaemia at visit 1 (state)
- $Y$ :  $\log HbA_{1c}$  measured at visit 2 (outcome) (final state)

2. Data generation process:

- $U_0 \sim \text{Bernoulli}(0.4)$
- $A_0 \sim \text{Bernoulli}(0.5)$  (randomized initial treatment)
- $L_1|U_0, A_0 \sim \text{Bernoulli}(P(L_1 = 1) = 0.25 + 0.3A_0 - 0.2U_0 - 0.05A_0U_0)$
- $A_1|A_0, L_1 \sim \text{Bernoulli}(P(A_1 = 1) = 0.4 + 0.5A_0 - 0.3L_1 - 0.4A_0L_1)$
- $Y|U_0, A_0, A_1 \sim \text{Normal}(\mu = 2.5 - 0.5A_0 - 0.75A_1 + 0.2A_0A_1 - U_0, \sigma = 0.2)$

We want to estimate the counterfactual mean of  $Y$  under different treatment strategies  $(a_0, a_1)$ .

The counterfactual means are calculated by averaging over the distribution of  $U_0$ :

$$\mathbb{E}[Y(a_0, a_1)] = 2.5 - 0.4 - 0.5a_0 - 0.75a_1 + 0.2a_0a_1. \quad (4.5)$$

Alternatively, given  $U_{0,i}$ , the potential outcomes  $Y_i(a_0, a_1)$  can be considered as being independently generated for each  $(a_0, a_1)$  and for each  $i$  from a normal distribution with a mean of  $2.5 - 0.5a_0 - 0.75a_1 + 0.2a_0a_1 + U_{0,i}$  and a standard deviation of 0.2.

In Figure 4.6 the SCM for the diabetes dataset is presented. We can notice that

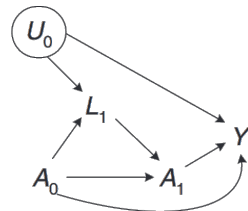


Figure 4.6: Structural Causal Model for the diabetes dataset.

Source: [Daniel et al., 2013]

the data generation model for  $A_0$  and  $A_1$  do not incorporate  $U_0$ , thus  $A_0 \perp\!\!\!\perp U_0$  and  $A_1 \perp\!\!\!\perp U_0|L_1$ . Because of this the variation in  $Y(a_0, a_1)$  is independent of all the other

random variables in the model, making  $A_0 \perp\!\!\!\perp Y(a_0, a_1)$  and  $A_1 \perp\!\!\!\perp Y(a_0, a_1) | A_0, L_1$ . Given this, the “no unmeasured confounding” assumption hold in this case.

The return value given to the RL agent in this environment is the negative value of  $Y$  at the end of the simulation.

This dataset captures key aspects of diabetes treatment, including:

- The effect of initial health status on anaemia risk and  $HbA_{1c}$  levels
- The potential side effect of antiglycaemic drugs causing anaemia
- The influence of anaemia on subsequent treatment decisions
- The causal effect of treatment on  $HbA_{1c}$  levels

In Figure 4.7, we present a tree depicting the expected values of the variables out of a total of 2000 subjects.

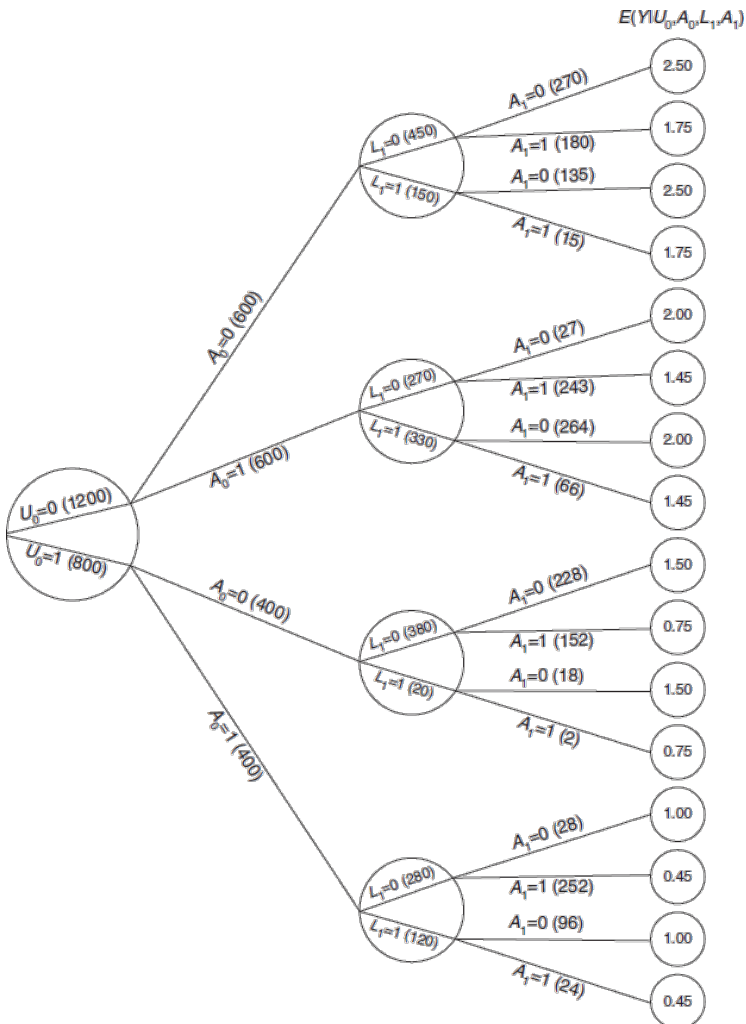


Figure 4.7: Tree diagram of the expected numbers along each branch for the distribution from which the diabetes dataset was generated.

Source: [Daniel et al., 2013]

## 4.3 Frameworks for Counterfactual Data Generation

In this section, we introduce two different approaches designed to address the challenges of training agents using Offline Deep Reinforcement Learning (DRL) with a pre-collected dataset  $\mathcal{D}$ . Both approaches aim to generate additional high-fidelity experiences that align with the environment’s underlying transition dynamics but differ in their methodologies and assumptions.

In the following subsections, we delve into the specifics of each approach, outlining their methodologies, advantages, and implementation details. This exploration aims to provide a comprehensive understanding of how these frameworks can be employed to augment the dataset  $\mathcal{D}$  and improve the training of offline DRL agents.

### 4.3.1 Wasserstein Reward-enhanced Counterfactual Data Generation

The first approach, called Wasserstein Reward-enhanced Counterfactual Data Generation (WRe-CTDG), focuses on inferring the Structural Causal Model (SCM) from the available data  $\mathcal{D}$  and simultaneously learning a function to estimate the unobserved variables  $U_{t+1}$ .

This approach is valuable when the underlying dynamics of the environment are complex and not fully known, allowing us to infer and utilize causal relationships for better training.

The proposed strategy for estimating the Structural Causal Model (SCM) integrates two key components: an optional Convolutional AutoEncoder (CAE) for dimensionality reduction and a Deep Generative Model for implementing the causal mechanisms.

The CAE is designed to compress high-dimensional visual inputs, making the data more manageable while retaining essential information. The Deep Generative Model is used to learn the causal mechanism  $f_s$ , the abduction function needed to estimate  $U_{t+1}$ , and the reward model  $f_r$ . Figure 4.8 provides a visual illustration of the entire solution.

#### Dimensionality Reduction via Convolutional AutoEncoders

Unlike state-of-the-art approaches, our work generates experience samples where states can also be represented by images. To handle the challenges posed by high-dimensional visual data, we present the possibility of using a CAE, which is a Variational AutoEncoder (VAE, see Section 2.2.1) made by two Convolutional Neural Networks (CNN, see Section 3.1.1). to compute low-dimensional encodings that preserve the meaningful information from the input images. It consists of an encoder  $\phi = E_s(\mathcal{I})$  that extracts a low-dimensional encoding  $\phi$  from the image  $\mathcal{I}$ , and a decoder  $D_s(\phi) = \mathcal{I}_{\text{rec}}$  that reconstructs the original image  $\mathcal{I}$ .

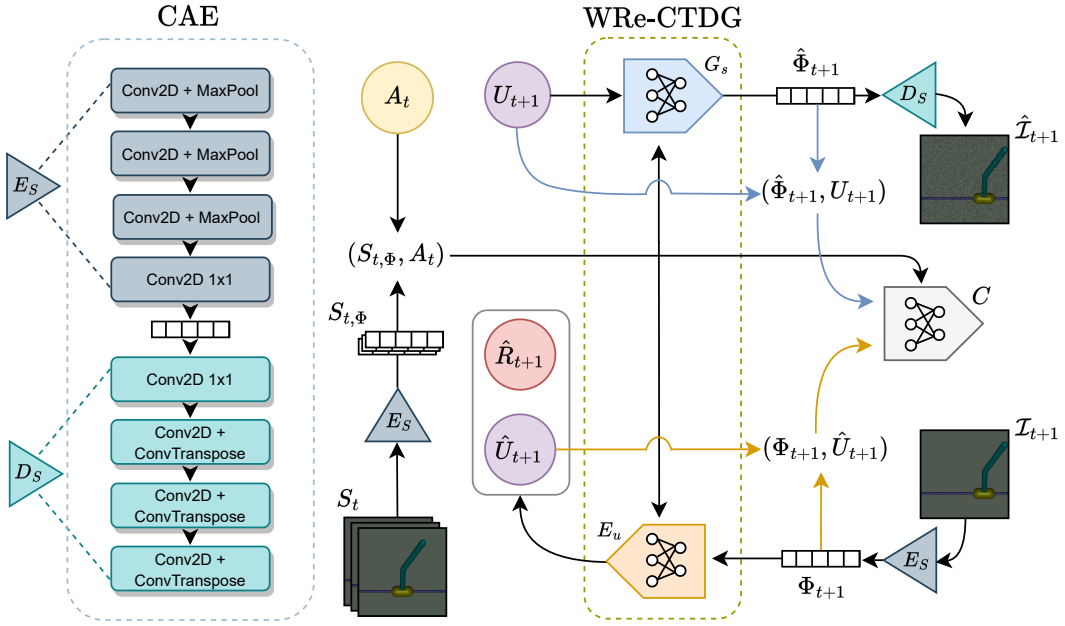


Figure 4.8: WRe-CTDG framework in a situation where the states are images only and the CAE is employed.

The CAE is trained by minimizing the reconstruction error over the images  $\mathcal{I}$  in the collected dataset  $\mathcal{D}$ :

$$\mathcal{L}_{E_s, D_s} = \mathbb{E}_{\mathcal{I} \sim P_{\text{data}}} [\|\mathcal{I} - \mathcal{I}_{\text{rec}}\|^2] \quad (4.6)$$

Minimizing this reconstruction error ensures that the encoder  $E_s$  computes robust and informative image encodings, and the decoder  $D_s$  can accurately reconstruct images from these encodings.

The encoder is used to encode the images representing the environment states into their corresponding low-dimensional encodings. We refer to the encoded states at time  $t$  and  $t + 1$  as  $s_{t,\phi} = E_s(s_t)$  and  $s_{t+1,\phi} = E_s(s_{t+1})$ . The decoder is used to reconstruct images from the low-dimensional encodings generated by the generator network. The weights of both  $E_s$  and  $D_s$  are frozen and not updated during the next phase of learning the SCM model.

In the next section we are not going to explicitly use  $s_{t,\phi}$  and  $s_{t+1,\phi}$  since utilizing the CAE is optional and depends on the nature of the state representation. So, by default, we will refer to the states as  $s_t$  and  $s_{t+1}$ .

### Counterfactual Data Generation

To learn the SCM from the collected dataset  $\mathcal{D}$ , we propose a novel strategy called Wasserstein Reward-enhanced Counterfactual Data Generation (WRe-CTDG). This solution builds upon the BiCoGAN framework presented in [Lu et al., 2020] with significant enhancements aimed at improving the effectiveness of the estimated SCM

in generating counterfactual samples in vision-based DRL problems. Key enhancements include adapting the Wasserstein Generative Adversarial Network (WGAN) framework (see Section 3.3.3) for improved training stability and introducing an additional loss term to learn the reward model and predict reward values for counterfactual actions.

The WRe-CTDG framework consists of three main components:

- **Generator  $G_s$ :** Implements the causal mechanism  $f_s$ . It maps the inputs  $(U_{t+1}, X_t)$  to the next-state encoding  $\hat{\phi}_{t+1}$ , where  $X_t = (S_t, A_t)$ . The distribution learned by  $G_s$  is  $P(\hat{\Phi}_{t+1}|U_{t+1}, X_t)$ .
- **Encoder  $E_u$ :** Implements the abduction function. It maps the inputs  $(\Phi_{t+1}, X_t)$  to the estimated unobserved factor  $\hat{u}_{t+1}$ . The distribution learned by  $E_u$  is  $P(\hat{U}_{t+1}|\Phi_{t+1}, X_t)$ . Additionally,  $E_u$  estimates the reward model  $f_r$  to predict the reward associated with a  $(\Phi_{t+1}, X_t)$  tuple, denoted as  $\hat{r}_{t+1}$ .
- **Critic  $C$ :** Integrates the WGAN paradigm into the framework. It replaces the discriminator in traditional GANs and computes a score quantifying the likelihood of the input tuples being drawn from either the joint distribution  $P(\hat{\Phi}_{t+1}, U_{t+1}, X_t)$  (generated samples) or  $P(\Phi_{t+1}, \hat{U}_{t+1}, X_t)$  (real samples).

The metric is approximated by the Wasserstein distance  $W$  as follows:

$$W = \mathbb{E}_{T \sim P_D} [C(\hat{\Phi}_{t+1}, U_{t+1}, X_t)] - \mathbb{E}_{T \sim P_D} [C(\Phi_{t+1}, \hat{U}_{t+1}, X_t)] \quad (4.7)$$

where  $C(\cdot)$  is a score computed by the critic.

The goal of training the encoder-generator pair is to minimize  $W$ , thereby improving the ability of both the encoder and generator to produce samples that are indistinguishable from those generated by their counterparts. Additionally, the function  $E_u$  must accurately predict the rewards for each transition. Thus, the objective function for the pair  $(G_s, E_u)$  is defined as:

$$L_{G_s, E_u} = -W + \lambda_R \mathbb{E}_{R_{t+1} \sim P_D} [\|\hat{R}_{t+1} - R_{t+1}\|^2] \quad (4.8)$$

where  $\lambda_R$  regulates the influence of the reward prediction term. On the other hand, the critic is trained using the Wasserstein Loss with Gradient Penalty, which addresses the problem of vanishing gradients and the limited expressive power of traditional WGANs [Gulrajani et al., 2017]. The objective function for  $C$  is defined as:

$$L_C = W + \lambda_G \mathbb{E}_{T \sim P_D} \left[ (\|\nabla_{\tilde{\Phi}_T, \tilde{U}_T} C(\tilde{\Phi}_T, \tilde{U}_T, X_T)\| - 1)^2 \right] \quad (4.9)$$

where  $\lambda_G$  determines the strength of the Gradient Penalty and the interpolation variables  $\tilde{\Phi}_T$  and  $\tilde{U}_T$  are given by:

$$\begin{aligned}\tilde{\Phi}_T &= \alpha \Phi_{t+1} + (1 - \alpha) \hat{\Phi}_{t+1} \\ \tilde{U}_T &= \alpha U_{t+1} + (1 - \alpha) \hat{U}_T\end{aligned}$$

for  $\alpha \in [0, 1]$ , sampled uniformly at random, indicating a blend between real and generated samples. By maximizing  $W$ , the critic aims to increase the difference in evaluations between samples generated from the generator distribution  $P(\hat{\Phi}_{t+1}|U_{t+1}, X_t)$  and those from the encoder distribution  $P(\hat{U}_{t+1}|\Phi_{t+1}, X_t)$ .

When the data is purely numerical or when the CAE is employed, both the Generator  $G_s$  and the Encoder  $E_u$  consist exclusively of fully connected layers. This architecture is sufficient to handle the numerical input and effectively capture the dependencies in the data. However, when the state representation includes images, convolutional layers are incorporated into both the Generator and the Encoder:

- In the Encoder, the convolutional blocks perform a downsampling on the images, effectively reducing their spatial dimensions while capturing essential features. These downsampled feature maps are then flattened and combined with the other numerical data, ensuring a comprehensive representation of the input.
- In the Generator, after extracting the numerical data, convolutional blocks are used to upsample the output of the fully connected network. This upsampling process reconstructs the spatial dimensions, enabling the model to generate the image  $\mathcal{I}_{t+1}$ .

### Experience Generation through Counterfactual Augmentation

After understanding the causal mechanism  $f_s$ , the abduction function, and the reward model  $f_r$ , we can utilize WRe-CTDG and (optionally) the CAE for counterfactual data augmentation. The original dataset  $\mathcal{D}$  is expanded by a factor of  $\beta$  according to the method described in Algorithm 1. Specifically, if the CAE is used, for each sampled tuple  $T = (s_t, s_{t+1}, a_t, r_{t+1}) \in D$ , the image encodings in  $s_t$ , so  $s_t['img'] = \{\mathcal{I}_{t-(N_S-1)}, \dots, \mathcal{I}_{t-1}, \mathcal{I}_t\}$ , and  $\mathcal{I}_{t+1} \in s_{t+1}$  are first computed using the encoder  $E_s$ . Next,  $E_u$  and  $G_s$  are used to create a counterfactual sample through three steps:

1. Perform abduction with  $E_u$  to estimate the unknown factor  $\hat{u}_{t+1}$ ;
2. Use  $G_s$  to generate the counterfactual states  $\hat{s}'_{t+1}$  given  $\hat{u}_{t+1}, s_t$ , and the counterfactual action  $a'_t$ ;
3. Use  $E_u$  again to produce the reward  $\hat{r}'_{t+1}$ .

Finally, if the CAE is used, the image  $\hat{\mathcal{I}}'_{t+1}$  is generated using the decoder  $D_s$ . Once the augmented dataset  $\mathcal{D}'$  is ready, it can be used to train any off-policy DRL algorithm, such as D3QN or TD3.

### 4.3.2 Supervised Counterfactual Data Generation

The second approach, called Supervised Counterfactual Data Generation (S-CTDG), assumes that the noise in the system is known in the training phase and focuses on directly collecting counterfactual states.

This approach shifts the problem towards creating the most accurate and representative simulator, enhancing the realism and diversity of the generated experiences. It is particularly useful when there is access to detailed knowledge about the noise in the system, even in just a subset of the available data, enabling a more precise simulation of the environment.

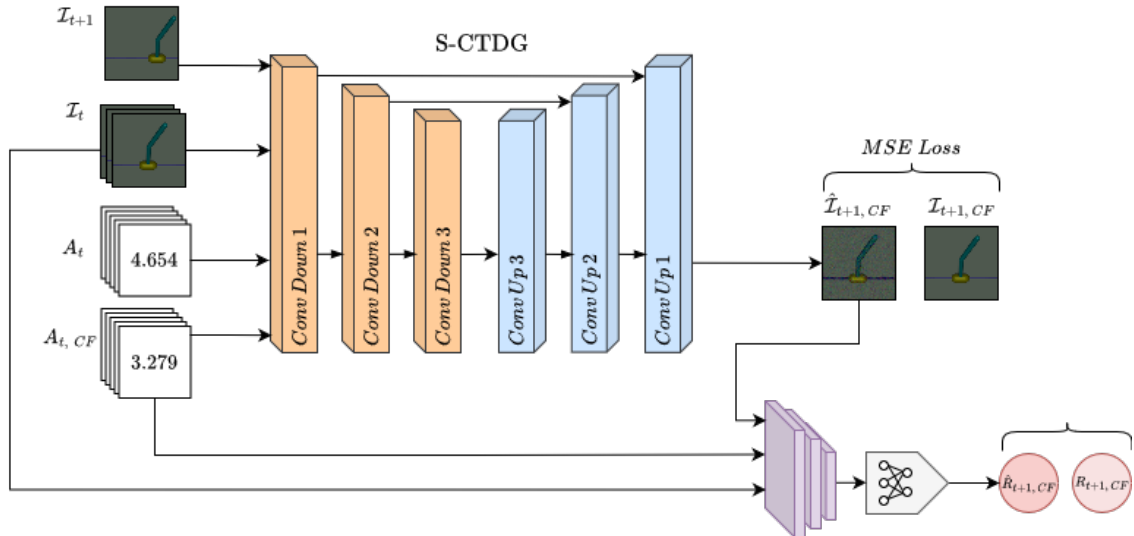


Figure 4.9: S-CTDG framework in a situation where the states are images only.

#### Counterfactual Data Generation

The current architecture of our network is designed to process unimodal data, specifically either image-based or numerical inputs. While the framework possesses the potential for extension to multimodal environments, the present implementation focuses on these two distinct data types.

For **numerical data** processing, the network employs a fully connected MLP. This network accepts as input the concatenation of the current state  $\mathcal{X}_t$ , the subsequent state  $\mathcal{X}_{t+1}$ , the action taken  $A_t$ , and the counterfactual action  $A_{t,CF} \neq A_t$ . The network then produces as output the estimated counterfactual next state  $\hat{\mathcal{X}}_{t+1,CF}$  and the corresponding counterfactual reward  $\hat{R}_{t+1,CF}$ .

For **image-based** inputs, we implement a CNN architecture with symmetric downsampling and upsampling paths, interconnected via skip connections. This structure is reminiscent of **U-Net** introduced in [Ronneberger et al., 2015], facilitating the preservation of spatial information. The network's input comprises the current state image  $\mathcal{I}_t$ , the subsequent state image  $\mathcal{I}_{t+1}$ , and image representations

of both the actual action  $A_t$  and the counterfactual action  $A_{t,CF} \neq A_t$ . The action-to-image conversion process is contingent on the nature of the action space:

- For **discrete**, one-hot encoded action spaces (e.g. Acrobot), each action is represented as a single-channel image where all pixels hold the same value derived from the encoding vector.
- For **continuous** action spaces (e.g. Half Cheetah), each action vector is transformed into a multi-channel image, where the  $i$ -th channel is a uniform grid populated with the  $i$ -th component of the action vector.

The network produces the counterfactual next state image  $\hat{\mathcal{I}}_{t+1,CF}$ , which is then processed, along with the current state image  $\mathcal{I}_t$  and the image representation of the counterfactual action  $\mathcal{A}_{t,CF}$ , by a subsequent, more compact CNN. This secondary network estimates the counterfactual reward  $\hat{R}_{t+1,CF}$ .

The loss function used to train the neural network is composed of two terms: the Mean Squared Error (MSE) between the predicted counterfactual state and the real counterfactual state and the MSE between the predicted counterfactual reward and the real counterfactual reward:

$$\mathcal{L} = \mathbb{E} \left[ (\hat{\mathcal{S}}_{t+1,CF} - \mathcal{S}_{t+1,CF})^2 \right] + \mathbb{E} \left[ (\hat{R}_{t+1,CF} - R_{t+1,CF})^2 \right] \quad (4.10)$$

where  $\mathcal{S}$  represents the state as either a numerical vector or an image.

The S-CTDG model takes as input the current state  $s_t$ , the next state  $s_{t+1}$ , the original action  $a_t$ , and the counterfactual action  $a'_t$ . It then produces a counterfactual next state  $\hat{s}'_{t+1}$  and a counterfactual reward  $\hat{r}'_{t+1}$ . This process effectively allows the algorithm to ask “what if?” questions about the environment, simulating alternative scenarios that didn’t actually occur but could have occurred if different actions had been taken.

### Experience Generation through Counterfactual Augmentation

After understanding the end-to-end causal mechanism of the S-CTDG model, we can utilize it for counterfactual data augmentation. The original dataset  $\mathcal{D}$  is expanded by a factor of  $\beta$  according to the method described in Algorithm 2. For each sampled tuple  $T = (s_t, s_{t+1}, a_t) \in \mathcal{D}$ , the process is simplified compared to the WRe-CTDG method. Instead of separate encoding and generation steps, the S-CTDG model  $G_{sup}$  directly generates the counterfactual state  $\hat{s}'_{t+1}$  and reward  $\hat{r}'_{t+1}$  given the current state  $s_t$ , next state  $s_{t+1}$ , current action  $a_t$ , and a randomly chosen counterfactual action  $a'_t$ . The abduction step here is implicit in the generation process. This end-to-end approach eliminates the need for explicit separate estimation of unknown factors. Once the augmented dataset  $\mathcal{D}'$  is ready, it can be used to train any off-policy DRL algorithm, such as D3QN or TD3.

---

**Algorithm 1:** WRe-CTDG + CAE Counterfactual Augmentation

---

**Input:** dataset  $\mathcal{D}$ , augmentation factor  $\beta > 1$ ,  
 $(E_s, D_s)$  CAE,  $(G_s, E_u)$  WRe-CTDG  
**Output:** augmented dataset  $\mathcal{D}'$

```

 $\mathcal{D}' \leftarrow \text{copy}(\mathcal{D})$ 
 $M \leftarrow \text{size of } \mathcal{D}$ 
 $M' = M \leftarrow \text{size of } \mathcal{D}'$ 
while  $M' < \beta M$  do
    Sample batch  $B \in \mathcal{D}$ 
     $B' \leftarrow \emptyset$ 
    foreach  $T = (s_t, s_{t+1}, a_t, r_{t+1}) \in B$  do
        if CAE is used then
             $s_t \leftarrow \text{encode images in } s_t: E_s(s_t)$ 
             $s_{t+1} \leftarrow \text{encode last image in } s_{t+1}: E_s(s_{t+1})$ 
            Abduction:  $\hat{u}_{t+1} \leftarrow E_u(s_{t+1}, s_t, a_t)$ 
            Action:  $a'_t \leftarrow \text{choose random action } \neq a_t$ 
            Prediction:  $\hat{s}'_{t+1} \leftarrow G_s(\hat{u}_{t+1}, s_t, a'_t)$ 
             $\hat{r}'_{t+1} \leftarrow E_u(\hat{s}'_{t+1}, s_t, a'_t)$ 
            if CAE is used then
                 $\hat{s}'_{t+1} \leftarrow \text{decode last generated image in } \hat{s}'_{t+1} : D_s(\hat{s}'_{t+1})$ 
            Insert  $T' = (s_t, \hat{s}'_{t+1}, a'_t, \hat{r}'_{t+1})$  in  $B'$ 
        Insert  $B'$  in  $\mathcal{D}'$ 
         $M' \leftarrow \text{size of } \mathcal{D}'$ 
    return  $\mathcal{D}'$ 

```

---



---

**Algorithm 2:** S-CTDG Counterfactual Augmentation

---

**Input:** dataset  $\mathcal{D}$ , augmentation factor  $\beta > 1$ ,  $G_{sup}$  S-CTDG  
**Output:** augmented dataset  $\mathcal{D}'$

```

 $\mathcal{D}' \leftarrow \text{copy}(\mathcal{D})$ 
 $M \leftarrow \text{size of } \mathcal{D}$ 
 $M' = M \leftarrow \text{size of } \mathcal{D}'$ 
while  $M' < \beta M$  do
    Sample batch  $B \in \mathcal{D}$ 
     $B' \leftarrow \emptyset$ 
    foreach  $T = (s_t, s_{t+1}, a_t) \in B$  do
        Action:  $a'_t \leftarrow \text{choose random action } \neq a_t$ 
        Prediction:  $(\hat{s}'_{t+1}, \hat{r}'_{t+1}) \leftarrow G_{sup}(s_t, s_{t+1}, a_t, a'_t)$ 
        Insert  $T' = (s_t, \hat{s}'_{t+1}, a'_t, \hat{r}'_{t+1})$  in  $B'$ 
    Insert  $B'$  in  $\mathcal{D}'$ 
     $M' \leftarrow \text{size of } \mathcal{D}'$ 
return  $\mathcal{D}'$ 

```

---

## Chapter 5

# Experiments

## 5.1 Hardware Specifications

All experiments were conducted on a high-performance PC with the following specifications:

- CPU: Intel Core i7-9800X CPU @ 3.80GHz, 3792 Mhz, 8 core, 16 threads
- GPU: 2 NVIDIA RTX 2080 Ti GPU with 12GB VRAM each
- RAM: 64 GB DDR4
- Storage: 1 TB Seagate BarraCuda HDD

## 5.2 Software Environment

The experiments were implemented using the following software stack:

- Operating System: Windows 11 Pro
- Python: 3.10.14
- PyTorch: 2.3.0
- CUDA: 12.0
- TorchRL: 0.4.0
- MuJoCo: 3.14

## 5.3 Network Architectures Details

### 5.3.1 WRe-CTDG Network Structure

The WRe-CTDG framework consists of three main components: Encoder  $E_u$ , Generator  $G_s$ , and Critic  $C$ . Here are the details of each network:

**Encoder  $E_u$ :**

- Input layer:  $2 \times$  numerical state dimensions +  $2 \times$  latent state dimensions + action dimension
- Hidden layers: 4 fully connected layers with 256, 512, 512, and 256 units respectively
- Output layer: noise dimension + 1 (for reward prediction)
- Activation function: ReLU for hidden layers, Tanh/Sigmoid/Identity for reward output, Linear for noise output

**Generator  $G_s$ :**

- Input layer: numerical state dimension + latent state dimension + action dimension + noise dimension
- Hidden layers: 4 fully connected layers with 256, 512, 256, and 128 units respectively
- Output layer: numerical state dimension + latent state dimension
- Activation function: ReLU for hidden layers, Linear for output layer

**Critic C:**

- Input layer:  $2 \times$  numerical state dimensions +  $2 \times$  latent state dimensions + action dimension + noise dimension
- Hidden layers: 4 fully connected layers with 256, 512, 256, and 128 units respectively
- Output layer: 1
- Activation function: ReLU for hidden layers, Linear for output layer

For environments with image inputs, we additionally used a Convolutional AutoEncoder architecture to encode and decode the state representations:

**Convolutional Encoder:**

- 5 downsampling blocks
- Each block contains 2-3 convolutional layers with BatchNorm and ReLU activation
- Number of filters increases progressively:

$$\text{in\_channels} \rightarrow \text{base} \rightarrow 2 \times \text{base} \rightarrow 4 \times \text{base} \rightarrow 8 \times \text{base} \rightarrow 16 \times \text{base}$$

with  $\text{base} = 8$ .

- MaxPool2D with kernel size  $2 \times 2$  and stride 2 for downsampling between blocks
- Final  $1 \times 1$  convolutional layer to reduce channel dimension to  $bn = 1$  (bottleneck)

**Convolutional Decoder:**

- Initial  $1 \times 1$  convolutional layer to expand channel dimension from  $bn$  to  $16 \times \text{base}$
- 5 upsampling blocks

- Each block contains 2-3 convolutional layers with BatchNorm and ReLU activation
- Number of filters decreases progressively:

$$16 \times base \rightarrow 8 \times base \rightarrow 4 \times base \rightarrow 2 \times base \rightarrow base \rightarrow in\_channels$$

with  $base = 8$ .

- Upsampling using transposed convolution with kernel size  $2 \times 2$  and stride 2
- Final layer uses Tanh activation

The encoder and decoder are symmetric, with the number of filters changing at each level.

### 5.3.2 S-CTDG Network Structure

The S-CTDG framework for **images** employs a network architecture consisting of two components: a convolutional U-Net for counterfactual image generation and a separate convolutional network with a fully connected head for reward prediction.

**U-Net:**

- 5 downsampling blocks and 5 upsampling blocks
- Each block contains 2-3 convolutional layers with BatchNorm and ReLU activation
- Number of filters increases progressively in downsampling:

$$\begin{aligned} in\_channels \times (1 + stack\_length) + 2 \times (action\_channels) \rightarrow \\ \rightarrow base \rightarrow 2 \times base \rightarrow 4 \times base \rightarrow 8 \times base \rightarrow 16 \times base \end{aligned}$$

where the first term is the stack of current and previous images concatenated along the channel dimension with the next state image and the action and counterfactual action images. The number of filters then decreases in upsampling:

$$\begin{aligned} 16 \times base \times 2 \rightarrow 8 \times base \times 2 \rightarrow 4 \times base \times 2 \rightarrow \\ \rightarrow 2 \times base \times 2 \rightarrow base \times 2 \rightarrow in\_channels \end{aligned}$$

with  $base = 64$ , in upsampling the filters are doubled since we concatenate the corresponding downsampling block.

- Convolution with kernel size  $3 \times 3$ , stride 1, and padding 1
- MaxPool2D with kernel size  $2 \times 2$  and stride 2 for downsampling between blocks
- Final layer uses a Softsign activation function

### Reward Prediction Network:

- 5 downsampling blocks
- Each block contains 2-3 convolutional layers with BatchNorm and ReLU activation
- Number of filters increases progressively in downsampling:

$$\begin{aligned} \text{in\_channels} \times (1 + \text{stack\_length}) + \text{action\_channels} &\rightarrow \text{base} \rightarrow \\ &\rightarrow 2 \times \text{base} \rightarrow 4 \times \text{base} \rightarrow 8 \times \text{base} \rightarrow 16 \times \text{base} \end{aligned}$$

where the first term is the stack of current and previous images concatenated along the channel dimension with the estimated counterfactual next state image and the counterfactual action image. As before,  $\text{base} = 64$ .

- Convolution with kernel size  $3 \times 3$ , stride 1, and padding 1
- MaxPool2D with kernel size  $2 \times 2$  and stride 2 for downsampling between blocks
- Final layer uses an Identity activation function

The S-CTDG framework for **numerical** data employs a network architecture consisting of a single fully connected network branched into two heads: one for counterfactual data generation and one for reward prediction. The network architecture is as follows:

- Input layer:  $2 \times$  numerical state dimensions  $+ 2 \times$  action dimension
- Hidden layers: 7 fully connected layers with 512, 512, 512 and 256 units respectively
- Output layer for counterfactual data generation: numerical state dimension, Linear activation function
- Output layer for reward prediction: 1, Identity activation function

### 5.3.3 Reinforcement Learning Algorithms (D3QN and TD3)

For the reinforcement learning algorithms, we used the following architectures:  
For discrete action spaces we used **D3QN**:

- Input layer: state dimension
- Hidden layers: 4 fully connected layers with 32, 64, 128 and 128 units respectively
- Output layer: action dimension

It is a **Dueling CNN DQNetwork** as presented in [Wang et al., 2016].

Then, for continuous action spaces we used **TD3**:

Actor:

- Input layer: state dimension
- Hidden layers: 3 fully connected layers with 32, 64, 128 and 128 units respectively
- Output layer: action dimension
- Activation function: ReLU for hidden layers, Tanh for output layer

Critic:

- Input layer: state dimension + action dimension
- Hidden layers: 3 fully connected layers with 32, 64, 128 and 128 units respectively
- Output layer: 1
- Activation function: ReLU for hidden layers, Linear for output layer

The actor and critic networks are modelled after the architectures presented in [Lillicrap et al., 2019].

## 5.4 Training Process Details

### 5.4.1 Dataset Generation

For each environment, we generated a dataset of transitions using a random policy. This dataset served as the basis for our counterfactual data generation and reinforcement learning experiments.

The number of transitions in the dataset was different for each environment:

- Acrobot: 20'000 transitions, observation stack length: 2
- Half Cheetah: 50'000 transitions, observation stack length: 4
- Ant: 50'000 transitions, observation stack length: 4
- Diabetes: 100 transitions, observation stack length: 1

### 5.4.2 Counterfactual Data Generation

We used both WRe-CTDG and S-CTDG frameworks to generate counterfactual data. The augmentation factor  $\alpha$  was set to 4, effectively quadrupling the size of the original datasets, except on the Diabetes environment where  $\delta = 8$  was used. Only a subset of the original dataset was used for generating counterfactual data.

Training parameters:

- Batch size: 32
- Optimizer: Adam (learning rate:  $1 \times 10^{-4}$ ,  $\beta_1$ : 0.5,  $\beta_2$ : 0.9)
- Number of iterations: 10'000 for WRe-CTDG, 100'000 for S-CTDG (both  $\approx 12$ h of training)
- Frame size for image-based environments:  $128 \times 128$

Size of the augmented datasets:

- Acrobot:  $10'000 \times \alpha = 40'000$  transitions
- Half Cheetah:  $10'000 \times \alpha = 40'000$  transitions
- Ant:  $10'000 \times \alpha = 40'000$  transitions
- Diabetes:  $20 \times \delta = 160$  transitions

### 5.4.3 Reinforcement Learning Training

We trained D3QN and TD3 algorithms on both the original and augmented datasets. The training process involved:

- Number of training steps: 1'000 for Acrobot, 2'000 for Half Cheetah, 3'000 for Ant, 8'000 for Diabetes
- Batch size: 256
- Discount factor ( $\gamma$ ): 0.99
- Optimizer: Adam (learning rate:  $1 \times 10^{-4}$ ,  $\beta_1$ : 0.0,  $\beta_2$ : 0.9)
- Exploration strategy:  $\epsilon$ -greedy with decay factor  $\tau = 0.005$

## 5.5 Results

### 5.5.1 Training the Variational Autoencoder

We trained the VAE with each one of the three different image-based environments: Acrobot, Half Cheetah, and Ant.

We trained the VAE using the Adam optimizer (learning rate:  $1 \times 10^{-4}$ ,  $\beta_1$ : 0.5,  $\beta_2$ : 0.9) and a batch size of 128. The model was trained for 10'000 iterations on the combined dataset from all three environments. We used the standard MSE loss for the reconstruction error with a weight mask to give less importance to the background pixels.

Table 5.1 presents the mean squared error (MSE) of the reconstruction loss for each environment after training:

Environment	Reconstruction MSE
Acrobot	1.364
Half Cheetah	13.539
Ant	14.294

Table 5.1: Mean Squared Error (MSE) of reconstruction loss for each environment

The VAE achieved a significantly lower reconstruction error on the Acrobot environment compared to Half Cheetah and Ant. This substantial difference in reconstruction capability is likely due to the simpler visual structure of Acrobot, while Half Cheetah and Ant present more complex visual features and dynamics.

While a successful Acrobot reconstruction is shown in Figure 5.4, the poor reconstruction capability for Half Cheetah and Ant is visually demonstrated in Figures 5.5 and 5.6, respectively.

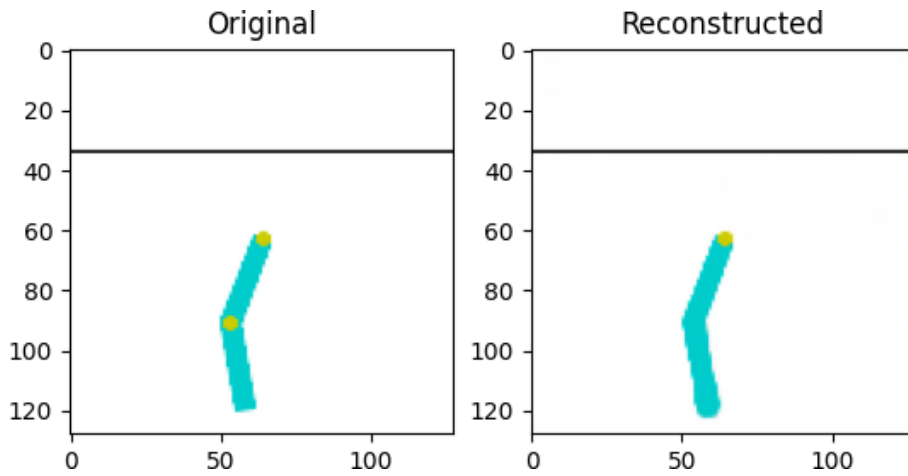


Figure 5.1: Acrobot Reconstruction

These results indicate that while the VAE successfully learned to encode and reconstruct images from all three environments, its performance varied significantly

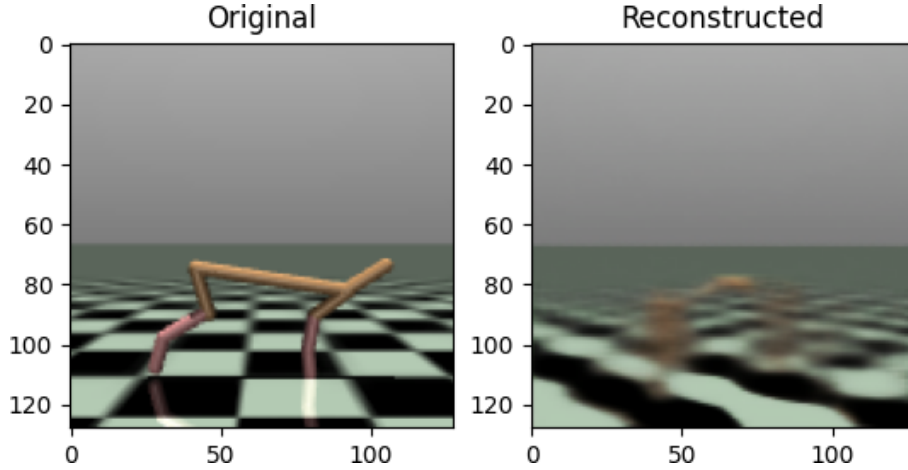


Figure 5.2: Half Cheetah Reconstruction

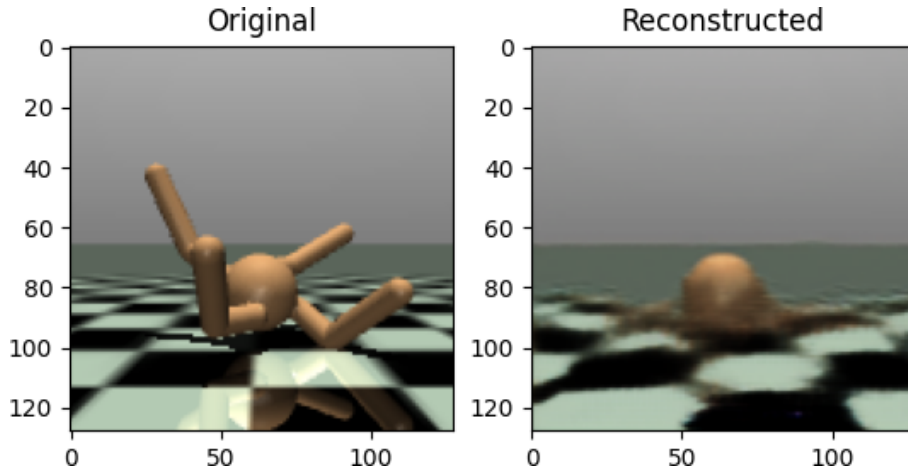


Figure 5.3: Ant Reconstruction

across them. The high reconstruction errors and poor visual quality for Half Cheetah and Ant suggest that the current VAE architecture may not be optimal for capturing the complex visual features of these environments. This limitation, as we will see, could have potentially impacted the effectiveness of using these learned latent representations in the subsequent reinforcement learning algorithms, particularly for the more visually complex environments.

### 5.5.2 Reconstruction Loss During Generation

We measured the Mean Absolute Error (MAE) on a validation set between the generated counterfactual states and the ground truth states after the training of WRe-CTDG (comparison between encoded values) and S-CTDG (comparison between images) frameworks as shown in Table 5.2.

The S-CTDG framework demonstrates superior reconstruction capabilities across all the image-based environments, as evidenced by the lower MAE values. To visu-

Environment	WRe-CTDG MAE	S-CTDG MAE
Acrobot	0.25189	0.00147
Half Cheetah	0.22064	0.03946
Ant	0.27296	0.09391
Diabetes	0.05602	0.12710

Table 5.2: WRe-CTDG and S-CTDG Reconstruction Loss

ally illustrate these reconstruction capabilities, we present a series of figures comparing original images to their S-CTDG reconstructions for each environment.

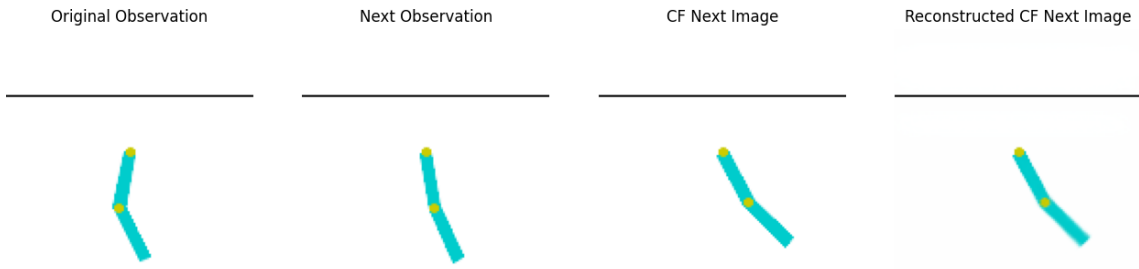


Figure 5.4: S-CTDG results for the Acrobot environment

Figure 5.4 showcases the S-CTDG reconstruction for the Acrobot environment. The remarkably low MAE is reflected in the near-perfect visual fidelity of the reconstructed image, with virtually no discernible differences from the original.

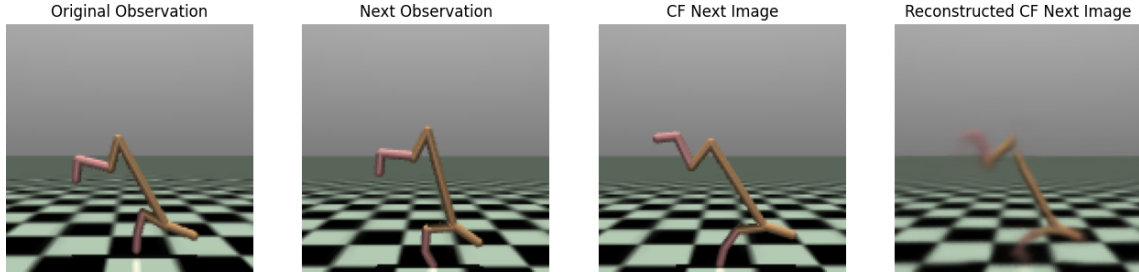


Figure 5.5: S-CTDG results for the Half Cheetah environment

The Half Cheetah environment reconstruction, shown in Figure 5.5, demonstrates the S-CTDG's ability to capture complex articulated structures. With an MAE of 0.03946, the reconstruction still maintains the overall structure and positioning of the ant, with some loss of sharpness in the finer details of the legs and joints.

Figure 5.6 illustrates the S-CTDG reconstruction for the Ant environment. Despite the higher MAE of 0.09391 compared to the previous environments, the reconstruction still captures the essential features of the ant's body and limbs, albeit with some loss of detail and sharpness.

For the Diabetes environment, as it doesn't involve image data, we do not provide

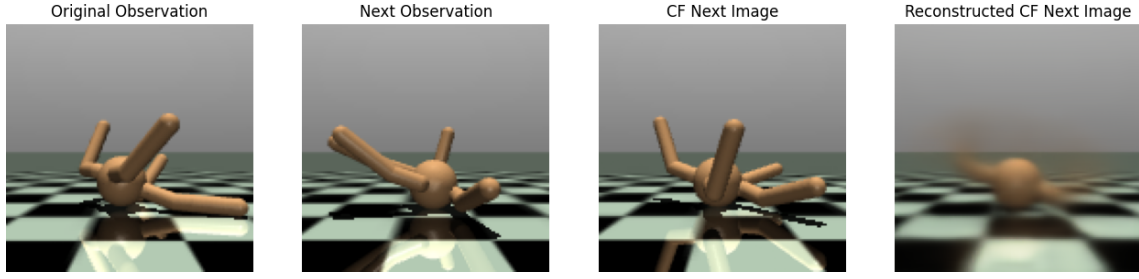


Figure 5.6: S-CTDG results for the Ant environment

a visual representation. However, it's worth noting that this is the only environment where WRe-CTDG outperforms S-CTDG in terms of MAE, likely due to the non-visual nature of the data.

### 5.5.3 Reinforcement Learning Performance

We evaluated the performance of D3QN and TD3 algorithms on both the original and augmented datasets. The results are presented in 5.3: the reward value shown is the best reward over all the evaluation episodes.

Environment	Algorithm	No Aug.	WRe-CTDG Aug.	S-CTDG Aug.
Acrobot	D3QN	-57.47	-53.35	-55.90
Half Cheetah	TD3	8.19	74.13	256.09
Ant	TD3	27.06	25.28	168.54
Diabetes	D3QN	0.04	0.06	0.12

Table 5.3: Reinforcement Learning Best Reward Value

In Figure 5.7 we show the reward trends for the Acrobot environment using D3QN, in the case of Half Cheetah, we show the reward trends in Figure 5.8, the trends of reward values for the Ant environment are shown in Figures 5.9 and, at last, the reward trends for the Diabetes environment are shown in Figures 5.10

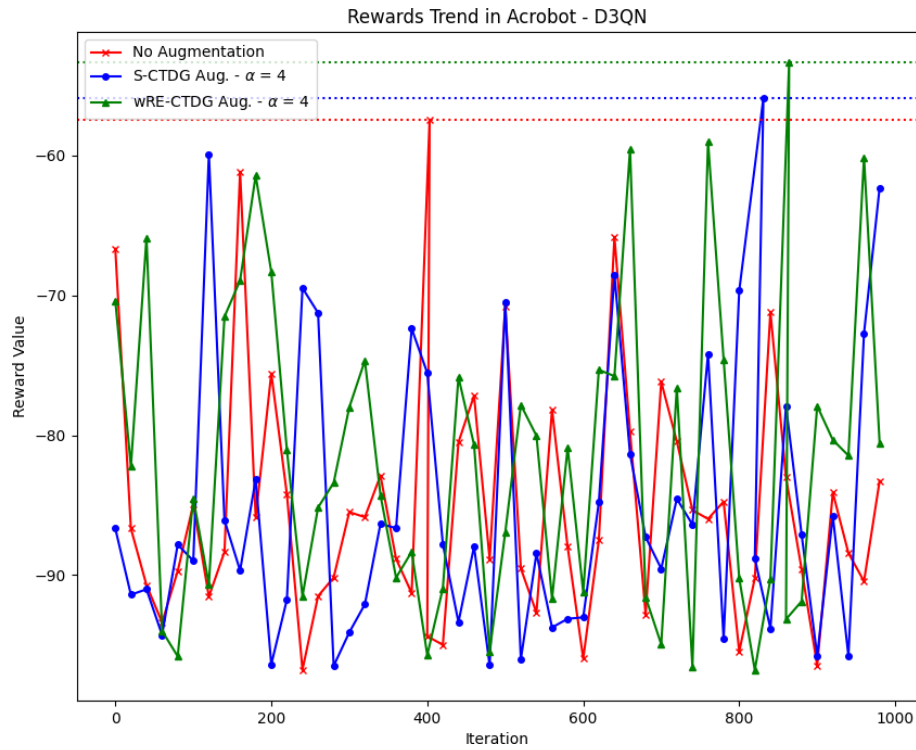


Figure 5.7: Acrobot Reward Trends

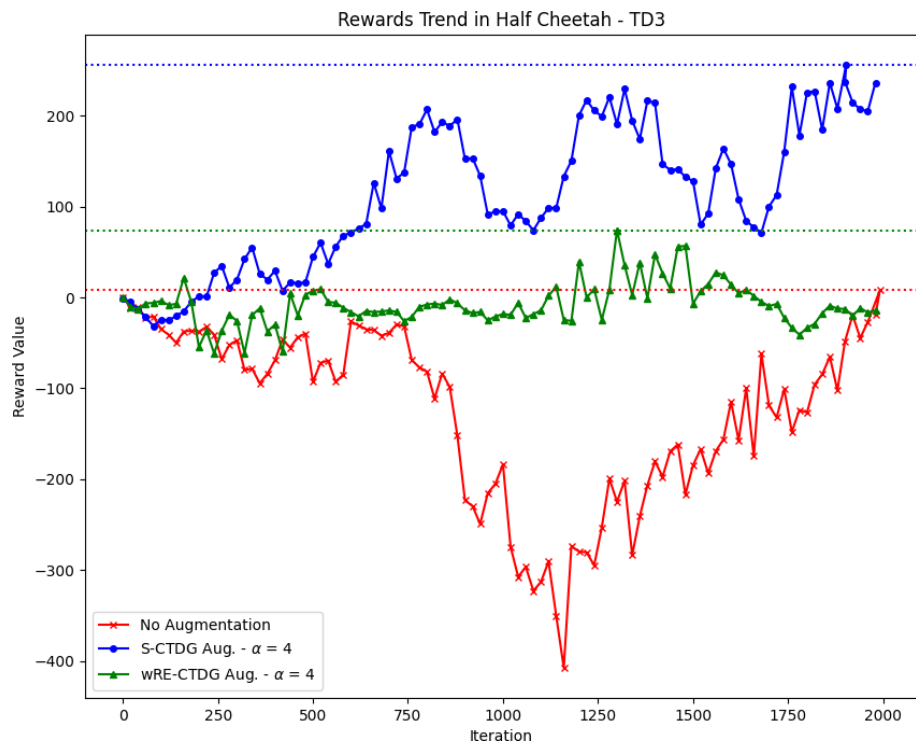


Figure 5.8: Half Cheetah Reward Trends

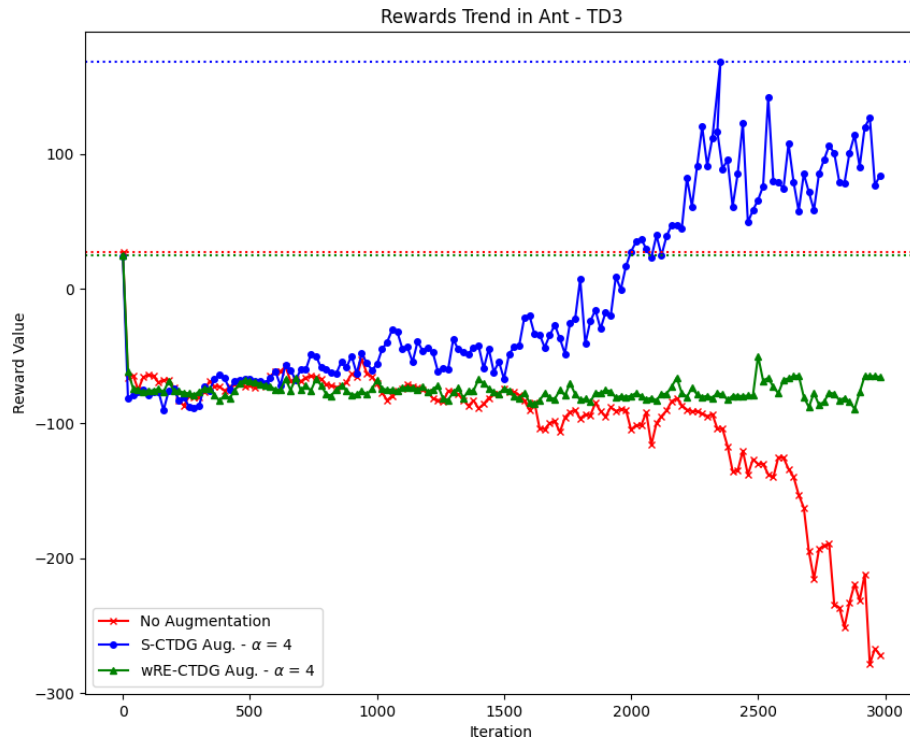


Figure 5.9: Ant Reward Trends

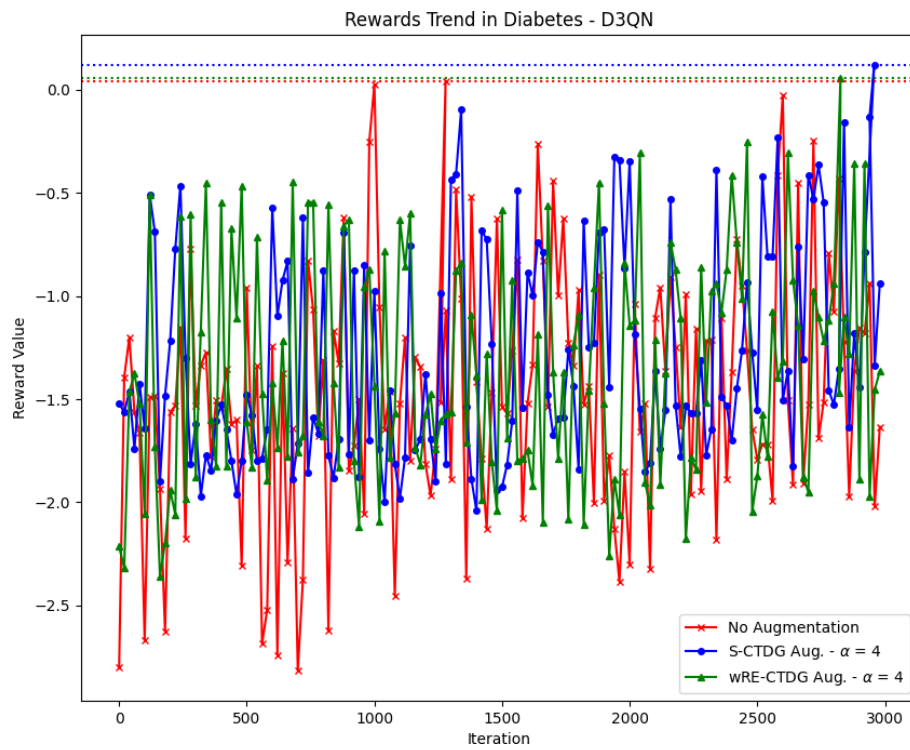


Figure 5.10: Diabetes Reward Trends

## 5.6 Discussion and Analysis of Results

These findings underscore the potential of counterfactual data generation, especially S-CTDG, in enhancing the performance of reinforcement learning algorithms across a variety of tasks and environments.

However, it is important to note that the effectiveness of S-CTDG comes with significant prerequisites and limitations:

1. **Prior knowledge of system noise:** S-CTDG requires prior knowledge of the noise affecting the system. This assumption may not always hold in real-world scenarios, where the exact nature and distribution of noise might be unknown or difficult to model accurately.
2. **Ability to perform counterfactual actions:** The S-CTDG method necessitates the ability to perform counterfactual actions during the data collection process. This requirement can be challenging or even impossible to meet in certain environments, particularly in real-world applications where data collection might be constrained by physical limitations, safety concerns, or ethical considerations.

These constraints highlight an essential trade-off: while S-CTDG demonstrates superior performance in our experiments, its applicability may be limited to scenarios where we have detailed knowledge of the system dynamics and full control over the data collection process. In contrast, methods like WRe-CTDG, while generally less effective, may be more broadly applicable as they don't impose such strict requirements on the data collection process or prior knowledge of the system.

# Chapter 6

# Conclusion

## 6.1 Summary of Findings

This thesis has explored novel approaches to address the challenges of data scarcity and noisy datasets in machine learning, with a specific focus on offline deep reinforcement learning scenarios. We introduced two frameworks for counterfactual data generation: the Wasserstein Reward-enhanced Counterfactual Data Generation (WRe-CTDG) and the Supervised Counterfactual Data Generation (S-CTDG).

Our experimental results demonstrated the efficacy of these frameworks across various environments and highlight the potential of counterfactual data generation in enhancing the performance of offline reinforcement learning algorithms in across diverse tasks and systems.

## 6.2 Implications and Contributions

The findings of this research have several important implications:

- **Improved Data Utilization:** Our frameworks demonstrate that it's possible to extract more value from existing datasets through sophisticated augmentation techniques, potentially reducing the need for extensive data collection.
- **Enhanced Model Performance:** The significant improvements in reward values, especially in complex environments like Half Cheetah and Ant, suggest that our methods can lead to more robust and effective reinforcement learning models.
- **Bridging Causal Inference and Machine Learning:** By incorporating Structural Causal Models and Generative Adversarial Networks, our work contributes to the growing field of causal machine learning, offering new ways to leverage causal relationships in data augmentation.
- **Applicability to Diverse Domains:** The effectiveness of our methods across both robotic simulations and healthcare scenarios indicates their potential broad applicability.

## 6.3 Limitations

Despite the promising results, it's important to acknowledge the limitations of our approach:

- **Prior Knowledge Requirement:** S-CTDG, while highly effective, requires prior knowledge of the system noise and the ability to perform counterfactual actions during data collection. This may limit its applicability in some real-world scenarios.

- **Computational Complexity:** The generation of counterfactual data, especially in complex environments, can be computationally intensive.
- **Generalization to Other Domains:** While our methods showed success in the tested environments, their effectiveness in other domains or more complex real-world scenarios remains to be fully explored.

## 6.4 Future Research Directions

Based on our findings and identified limitations, several avenues for future research emerge:

- **Relaxing Prior Knowledge Requirements:** Investigating methods to reduce the dependence on detailed prior knowledge of system dynamics could broaden the applicability of S-CTDG.
- **Scaling to More Complex Environments:** Exploring the effectiveness of these frameworks in increasingly complex and realistic environments would be valuable.
- **Real-World Applications:** Applying these techniques to real-world offline reinforcement learning problems to validate their practical utility.
- **Exploring Advanced ML Architectures:** Investigating the integration of state-of-the-art machine learning frameworks and structures, such as transformers (introduced in [Vaswani et al., 2023]) and diffusion models (presented in [Sohl-Dickstein et al., 2015]), into our counterfactual data generation approaches, for instance:
  - **Transformer**-based models, could improve the capture of long-range dependencies in sequential data, potentially leading to more coherent and realistic counterfactual trajectories.
  - **Diffusion models** might offer a new approach to generating high-quality counterfactual images, particularly in visually complex environments like robotics simulations.

In conclusion, this thesis has demonstrated the potential of causal inference-based counterfactual data generation in addressing challenges of data scarcity and noise in offline reinforcement learning. While there are limitations to be addressed, the promising results open up exciting possibilities for future research and applications in this rapidly evolving field.

# Bibliography

- [Andersen et al., 2018] Andersen, P.-A., Goodwin, M., and Granmo, O.-C. (2018). The dreaming variational autoencoder for reinforcement learning environments.
- [Bishop, 2008] Bishop, C. M. (2008). *Pattern Recognition and Machine Learning*. Springer-Verlag, New York.
- [Brockman et al., 2016] Brockman, G., Cheung, V., Pettersson, L., Schneider, J., Schulman, J., Tang, J., and Zaremba, W. (2016). Openai gym.
- [Chevtchenko et al., 2023] Chevtchenko, S., Bethi, Y., Ludermir, T., and Afshar, S. (2023). A neuromorphic architecture for reinforcement learning from real-valued observations.
- [Daniel et al., 2013] Daniel, R., Cousens, S., De Stavola, B., Kenward, M. G., and Sterne, J. A. C. (2013). Methods for dealing with time-dependent confounding. *Statistics in Medicine*, 32(9):1584–1618.
- [De Lazcano, 2022] De Lazcano, R. (2022). Inconsistent descriptions in half cheetah v4.py - GitHub. <https://github.com/openai/gym/issues/2932>. Accessed: 23-07-2024.
- [Donahue et al., 2017] Donahue, J., Krähenbühl, P., and Darrell, T. (2017). Adversarial feature learning.
- [Farama Org., 2023a] Farama Org. (2023a). Acrobot - Gymnasium Documentation. [https://gymnasium.farama.org/environments/classic\\_control/acrobot/](https://gymnasium.farama.org/environments/classic_control/acrobot/). Accessed: 05-08-2024.
- [Farama Org., 2023b] Farama Org. (2023b). Ant - Gymnasium Documentation. <https://gymnasium.farama.org/environments/mujoco/ant/>. Accessed: 23-07-2024.
- [Farama Org., 2023c] Farama Org. (2023c). Half Cheetah - Gymnasium Documentation. [https://gymnasium.farama.org/environments/mujoco/half\\_cheetah/](https://gymnasium.farama.org/environments/mujoco/half_cheetah/). Accessed: 23-07-2024.
- [Fujimoto et al., 2018] Fujimoto, S., van Hoof, H., and Meger, D. (2018). Addressing function approximation error in actor-critic methods.

- [Giorgetti et al., 2024] Giorgetti, F., Ferrante, F., and Fravolini, M. L. (2024). Anti-windup-like compensator design for continuous-time systems affected by unknown nonlinearities and input saturation. (*Submitted for publication*).
- [Goodfellow et al., 2016] Goodfellow, I., Bengio, Y., and Courville, A. (2016). *Deep Learning*. Adaptive computation and machine learning. MIT Press.
- [Goodfellow et al., 2014] Goodfellow, I. J., Pouget-Abadie, J., Mirza, M., Xu, B., Warde-Farley, D., Ozair, S., Courville, A., and Bengio, Y. (2014). Generative adversarial networks.
- [Gulrajani et al., 2017] Gulrajani, I., Ahmed, F., Arjovsky, M., Dumoulin, V., and Courville, A. (2017). Improved training of wasserstein gans.
- [Gürtler et al., 2023] Gürtler, N., Blaes, S., Kolev, P., Widmaier, F., Wüthrich, M., Bauer, S., Schölkopf, B., and Martius, G. (2023). Benchmarking offline reinforcement learning on real-robot hardware.
- [Ha and Schmidhuber, 2018] Ha, D. and Schmidhuber, J. (2018). World models.
- [Hafner et al., 2020] Hafner, D., Lillicrap, T., Ba, J., and Norouzi, M. (2020). Dream to control: Learning behaviors by latent imagination.
- [Han and Kim, 2022] Han, J. and Kim, J. (2022). Selective data augmentation for improving the performance of offline reinforcement learning.
- [Hansen and Wang, 2021] Hansen, N. and Wang, X. (2021). Generalization in reinforcement learning by soft data augmentation.
- [Hornik et al., 1989] Hornik, K., Stinchcombe, M., and White, H. (1989). Multilayer feedforward networks are universal approximators. *Neural Networks*, 2(5):359–366.
- [Jaiswal et al., 2018] Jaiswal, A., AbdAlmageed, W., Wu, Y., and Natarajan, P. (2018). Bidirectional conditional generative adversarial networks.
- [Joo et al., 2022] Joo, H.-T., Baek, I.-C., and Kim, K.-J. (2022). A swapping target q-value technique for data augmentation in offline reinforcement learning. *IEEE Access*, 10:57369–57382.
- [Kingma and Welling, 2022] Kingma, D. P. and Welling, M. (2022). Auto-encoding variational bayes.
- [Kumar et al., 2021] Kumar, A., Singh, A., Tian, S., Finn, C., and Levine, S. (2021). A workflow for offline model-free robotic reinforcement learning.
- [Laskin et al., 2020] Laskin, M., Lee, K., Stooke, A., Pinto, L., Abbeel, P., and Srinivas, A. (2020). Reinforcement learning with augmented data.

- [Lillicrap et al., 2019] Lillicrap, T. P., Hunt, J. J., Pritzel, A., Heess, N., Erez, T., Tassa, Y., Silver, D., and Wierstra, D. (2019). Continuous control with deep reinforcement learning.
- [Lin et al., 2020] Lin, Y., Huang, J., Zimmer, M., Guan, Y., Rojas, J., and Weng, P. (2020). Invariant transform experience replay: Data augmentation for deep reinforcement learning. *IEEE Robotics and Automation Letters*, 5(4):6615–6622.
- [Liu et al., 2023] Liu, Z., Guo, Z., Lin, H., Yao, Y., Zhu, J., Cen, Z., Hu, H., Yu, W., Zhang, T., Tan, J., and Zhao, D. (2023). Datasets and benchmarks for offline safe reinforcement learning.
- [Lu et al., 2020] Lu, C., Huang, B., Wang, K., Hernández-Lobato, J. M., Zhang, K., and Schölkopf, B. (2020). Sample-efficient reinforcement learning via counterfactual-based data augmentation.
- [Mertes et al., 2022] Mertes, S., Huber, T., Weitz, K., Heimerl, A., and André, E. (2022). Ganterfactual—counterfactual explanations for medical non-experts using generative adversarial learning. *Frontiers in Artificial Intelligence*, 5.
- [Mirza and Osindero, 2014] Mirza, M. and Osindero, S. (2014). Conditional generative adversarial nets.
- [Mnih et al., 2013] Mnih, V., Kavukcuoglu, K., Silver, D., Graves, A., Antonoglou, I., Wierstra, D., and Riedmiller, M. (2013). Playing atari with deep reinforcement learning.
- [Mumuni and Mumuni, 2022] Mumuni, A. and Mumuni, F. (2022). Data augmentation: A comprehensive survey of modern approaches. *Array*, 16:100258.
- [Neal, 2020] Neal, B. (2020). Introduction to causal inference.
- [OpenAI Inc., 2018] OpenAI Inc. (2018). Spinning Up documentation. [https://spinningup.openai.com/en/latest/spinningup/r1\\_intro2.html](https://spinningup.openai.com/en/latest/spinningup/r1_intro2.html). Accessed: 30-06-2024.
- [Pearl, 1988] Pearl, J. (1988). *Probabilistic Reasoning in Intelligent Systems: Networks of Plausible Inference*. Morgan Kaufmann Publishers Inc., San Francisco, CA, USA.
- [Ronneberger et al., 2015] Ronneberger, O., Fischer, P., and Brox, T. (2015). U-net: Convolutional networks for biomedical image segmentation. In *International Conference on Medical image computing and computer-assisted intervention*, pages 234–241. Springer.
- [Sauer and Geiger, 2021] Sauer, A. and Geiger, A. (2021). Counterfactual generative networks.

- [Shin and Kim, 2023] Shin, W. and Kim, Y. (2023). Guide to control: Offline hierarchical reinforcement learning using subgoal generation for long-horizon and sparse-reward tasks. In Elkind, E., editor, *Proceedings of the Thirty-Second International Joint Conference on Artificial Intelligence, IJCAI-23*, pages 4217–4225. International Joint Conferences on Artificial Intelligence Organization. Main Track.
- [Sohl-Dickstein et al., 2015] Sohl-Dickstein, J., Weiss, E. A., Maheswaranathan, N., and Ganguli, S. (2015). Deep unsupervised learning using nonequilibrium thermodynamics.
- [Sutton and Barto, 1998] Sutton, R. S. and Barto, A. G. (1998). *Reinforcement Learning: An Introduction*. The MIT Press.
- [Todorov et al., 2012] Todorov, E., Erez, T., and Tassa, Y. (2012). Mujoco: A physics engine for model-based control. In *2012 IEEE/RSJ International Conference on Intelligent Robots and Systems*, pages 5026–5033. IEEE.
- [van Hasselt et al., 2015] van Hasselt, H., Guez, A., and Silver, D. (2015). Deep reinforcement learning with double q-learning.
- [Vaswani et al., 2023] Vaswani, A., Shazeer, N., Parmar, N., Uszkoreit, J., Jones, L., Gomez, A. N., Kaiser, L., and Polosukhin, I. (2023). Attention is all you need.
- [Venuto et al., 2020] Venuto, D., Chakravorty, J., Boussoux, L., Wang, J., McCracken, G., and Precup, D. (2020). oirl: Robust adversarial inverse reinforcement learning with temporally extended actions.
- [Wang et al., 2022] Wang, K., Zhao, H., Luo, X., Ren, K., Zhang, W., and Li, D. (2022). Bootstrapped transformer for offline reinforcement learning.
- [Wang et al., 2016] Wang, Z., Schaul, T., Hessel, M., van Hasselt, H., Lanctot, M., and de Freitas, N. (2016). Dueling network architectures for deep reinforcement learning.
- [Zhao, 2024] Zhao, S. (2024). *Mathematical Foundations of Reinforcement Learning*. Springer Nature Press.